Controlling carbon formation over Ni/CeO2 catalyst for dry reforming of CH4 by tuning Ni crystallite size and oxygen vacancies of the support

Renata O. da Fonseca, Antonella R. Ponseggi, Raimundo C. Rabelo-Neto, Rita C. C. Simoes, Lisiane V. Mattos, Fabio Bellot Noronha

Controlling carbon formation over Ni/CeO_2 catalyst for dry reforming of CH_4 by tuning Ni crystallite size and oxygen vacancies of the support

Renata O. da Fonseca[1,2], Antonella R. Ponseggi [3], Raimundo C. Rabelo-Neto[2], Rita C.C. Simões[3], Lisiane V. Mattos[3], Fabio B. Noronha[1,2,4]*

[1] Military Institute of Engineering, Chemical Engineering Department, Praça Gal. Tiburcio 80, Rio de Janeiro, 22290-270, Brazil

[2] National Institute of Technology, Catalysis Division, Av. Venezuela 82, Rio de Janeiro, 20081-312, Brazil

[3] Fluminense Federal University, Chemical Engineering and Petroleum Department, Rua Passo da Pátria, 156, Niterói 24210-240, Brazil

[4] Université de Lille, CNRS, Centrale Lille, Université Artois, UMR 8181 – UCCS – Unité de Catalyse et Chimie du Solide, Lille, 59000, France.

* Corresponding author: e-mail: fabio.bellot@int.gov.br

Submitted to Journal of CO_2 utilization

Revised

December 2021

Abstract

This work investigates the effect of Ni crystallite size and oxygen vacancies of the support on the formation of carbon over Ni/CeO_2 catalysts for dry reforming of methane at 1073 K. A large crystallite size variation is achieved by using different Ni loading (5 and 10wt%) and calcination temperatures (673, 873, 1073 and 1473 K). *In situ* XRD and XANES experiments reveal that the increase in calcination temperature increases the Ni crystallite size, whereas the amount of oxygen vacancies decreases. The amount of carbon formed during DRM increases as Ni crystallite size increases, achieving a maximum at around 20-30 nm and then, it continuously decreases. However, carbon deposition is negligeable below 10 nm and above 100 nm. For the catalysts with very large Ni crystallite sizes, the CH_4 dissociation rate is likely so low that carbon species formed reacts and carbon accumulation does not take place. However, the oxygen vacancies of ceria do not contribute to the carbon removal from the Ni surface due to the low metal-support interface on these large Ni particles.

Keywords: CO_2 reforming of methane; Biogas; Nickel; Carbon formation; Particle size.

1. Introduction

The emission of biogas, produced by the anaerobic digestion of organic matter, into the atmosphere can contribute significantly to the greenhouse effect. Thus, several alternatives for the use of biogas have been proposed such as: (a) hydrogen production for proton exchange membrane fuel cells and; (b) energy generation through solid oxide fuel cells operating directly with biogas (DIR-SOFC).

In the first approach, biogas is converted into synthesis gas by the reaction of methane with CO_2 (DRM), followed by several H_2 purification steps (water gas-shift reaction, selective partial oxidation, methanation). Concerning DIR-SOFC, biogas is reformed on the SOFC anode, producing H_2 and CO, without the use of an external reformer or purification steps. These systems exhibit high efficiency even in small size power generations (<20 kW) and low sensitivity to impurities. In addition, high biogas conversions at the anode sides can be achieved due to the H_2 consumption by the electrochemical reaction [1-4]. However, one of the main challenges of DIR-SOFC is carbon deposition on the anode during the operation with biogas, which causes the rapid degradation of the DIR-SOFC performance. [5-10].

Ni-supported materials have been widely used as anodes for DIR-SOFC. However, the components of these devices are submitted to calcination at very high temperatures (1473 K) during the preparation of SOFC cells. Moreover, the typical operating temperature of SOFC cells is 1123 K, even when a catalytic layer (cathode / electrolyte / anode / catalyst) is used. These high temperatures employed for the synthesis of the cell and for the SOFC operation produces anodes containing large Ni particle size, which might be responsible for the deposition of carbon that causes deactivation of the anode. According to the literature [11], the presence of large metallic particles favors the formation of carbon over metal surface for the methane reforming

reactions. Thus, the size of Ni crystallite plays an important role on the formation of carbon during the operation of DIR-SOFC fueled with biogas.

One of the strategies to avoid carbon formation during DRM is the use of anodes containing CeO_2 as support. This is the so-called low temperature SOFC that operates at lower temperatures (873 - 1073 K) [12]. The use of CeO_2 as a support for Ni catalysts inhibits Ni particle sintering and thus, decreases carbon formation during DRM [13]. Furthermore, ceria-based oxides have a high oxygen mobility and participates in the dissociative adsorption of CO_2 near the metal particles, transferring oxygen to the surface of the metallic particle containing carbon deposits. This promotes the carbon removal mechanism, inhibiting the deactivation of the catalysts during the DRM reaction [14-18]. Marinho et al [13] investigated the effect of the preparation method on the resistance of Ni sintering for DRM. According to the authors, when Ni particles were embedded in the ceria, there was an increase in the interaction of Ni particles with CeO_2 and CeZr, which resulted in an increase in the number of oxygen vacancies and stabilization of Ni particles. Thus, this material more resistant to carbon deposition and sintering.

Although several works have investigated the use of Ni supported on ceria-based oxides as catalysts for DRM [14,18-21] only few studies have evaluated the performance of Ni/CeO_2 as a component of anodes for SOFC running on methane and CO_2 [5-7,22-24]. Unal et al [7] evaluated the performance of $Ni_{1-x}Co_x$/GDC catalyst layer in methane reforming for SOFC cells and also verified deactivation of catalysts during DRM at 1023 K caused by coke deposition. Santoro et al [5] studied Ni-based samarium doped ceria catalysts (Ni/SmDC) in DRM for indirect internal reforming of SOFC cells. SEM images of used anodes revealed the presence of carbon filaments that were responsible for the loss of active Ni sites, which was the main reason for catalysts deactivation during DRM. However, the effect of the calcination temperature and Ni

particle size on the carbon formation rate for DRM was also not evaluated on these studies.

Thus, the aim of this work is to study the relationship between Ni crystallite size and oxygen vacancies of the support with the carbon deposition rate over Ni/CeO_2 catalysts for DRM reaction. Catalysts with different Ni loading (5 and 10wt%) and calcination temperature (673, 873, 1073 and 1473 K) were prepared to obtain a wide range of Ni crystallite size. *in situ* X-ray diffraction (XRD) followed the changes in the Ni^0 crystallite size during reduction. *in situ* X-ray absorption near edge structure (XANES) at Ni K-edge and Ce L_{III}- edge determined the nickel and ceria reduction degree. The nature and the amount of carbon deposited on the catalysts during DRM reaction were obtained by scanning electron microscopy (SEM) and temperature-programmed oxidation (TPO) analysis. The results of this work give insights about the design of optimal anodes for the DIR-SOFC fueled with biogas.

2. Material and methods

2.1. Catalysts preparation

The hydrothermal method was used for the preparation of CeO_2 [25,26]. Briefly, cerium was precipitated from an aqueous solution containing cerium (IV) ammonium nitrate by the addition of an excess of ammonium hydroxide. After precipitation, the sample was heated at 453 K for 4h in an autoclave, followed by calcination at 573 K for 2h in a muffle (CeO_2_573). The catalysts were prepared by wet impregnation of the precursor CeO_2_573 with an aqueous solution of $Ni(NO_3)_2.6H_2O$ to obtain nominal loadings of 5 and 10 wt% of Ni. The impregnated samples were dried at 373 K for 24 h and then calcined at different temperatures (673, 873, 1073 or 1473K) for 5 h in a temperature-programmed muffle furnace with a heating rate of 2 K min^{-1}. The samples were denoted as 5Ni/CeO_2_673, 10Ni/CeO_2_673, 10Ni/CeO_2_873, 10Ni/CeO_2_1073 and 10Ni/CeO_2_1473. Commercial NiO (Sigma-Aldrich) was used as bulk NiO catalyst reference. For comparison, the supports were also prepared by calcination of CeO_2_573 at different temperatures (673, 873, 1073 or 1473K) under the same conditions used for the catalysts. These samples were designed as CeO_2_673, CeO_2_673, CeO_2_873, CeO_2_1073 and CeO_2_1473.

2.2. Raman spectroscopy (RAMAN)

Raman spectra were recorded on a Horiba/Jobin Yvon spectrometer, model LabRAM 800 equipped with an Olympus confocal microscope, model BX40, coupled to a CCD detector. The excitation wavelength of 632 nm was obtained from a He/Ne gas laser.

2.3. in situ X-ray diffraction (XRD)

in situ XRD experiments were performed at the beamline XRD1-D12A of the Brazilian Synchroton Light Laboratory (LNLS), Campinas, Brazil. The diffraction patterns were obtained with the Mythen-24 detector (Dectris), located in a circle at 760 mm from the sample. The scanning 2θ range was 10 - 120º, with an acquisition time of 150 s and a wavelength of 1.0332 Å. The measurements were performed during the reduction of the samples under a flow of pure H_2 (8 $mL.min^{-1}$), from 298 K to 1073 K, with a heating rate of 10 $K.min^{-1}$, remaining at the final temperature for 1 h. The average size of CeO_2, NiO and Ni^0 crystallites on the catalysts was estimated from Williamson-Hall 's equation that is more appropriated for large crystallites [27,28]:

$$\beta_{(hkl)}.\cos(\theta) = 4\varepsilon.\sin\theta + (k.\lambda/d) \quad (1)$$

where $\beta_{(hkl)}$ is the full width at half maximum of the peak with corrected instrumental broadening; θ is the position (angle) of the peak; k is the particle shape factor, taken as 0.9; λ is the incident X-ray wave length, ε is the microstrain, calculated from the slope of the curve of $\beta.\cos(\theta)$ versus $4\varepsilon.\sin\theta$ and the crystallite size (d) is obtained from the interception of the curve with the X axis.

2.4. X-ray diffraction (XRD)

XRD experiments were conducted after reduction at 1073K and passivation to obtain the crystallite size of Ni^0 for 5Ni/CeO_2_673 and 10Ni/CeO_2_873 catalysts. The XRD measurements were performed on a Bruker ASX D8 diffractometer with CuK_α radiation (λ = 1.5406 Å). The diffraction patterns were collected over the 2θ range of 20 to 100° using a scan rate of 0.02 degree $step^{-1}$ and a scan time of 1 s $step^{-1}$.

The samples were reduced at 1073 K under pure hydrogen (30 mL min^{-1}) for 1 h. Then, the catalysts were purged at this same temperature under N_2 for 30 min and cooled to 298 K. Then, the samples were passivated with a 0.5% O_2/N_2 mixture for 24 h at 298 K.

2.5. in situ X-ray absorption near edge structure (XANES)

in situ XANES spectra were measured at the D08B-XAFS-2 and D06A-DXAS beamline of the above-mentioned LNLS synchrotron facility. The samples were diluted with boron nitride, used as inert, and pressed to obtain a pellet. The XANES spectra were collected at the Ce L_{III}-edge (E_0 = 5.723 keV) and Ni K-edge (E_0 = 8.333 keV), while the samples were reduced under a 5% H_2 / He mixture from 298 K to 1073 K (10 $K.min^{-1}$), remaining at 1073 K for 1 h. The data were processed through the ATHENA software and the fractions of Ce^{4+}/Ce^{3+} and metallic Ni/NiO were estimated by the linear combination of the normalized XANES spectra at the Ce L_{III}-edge and Ni K-edge, using CeO_2 and Ce $(CH_3CO_2)_3$, and NiO and Ni foil as references, respectively.

2.6. Scanning electron microscopy (SEM)

SEM analyses of the spent catalysts after DRM for 24 h of TOS was performed on an INSPECT S/FEI microscope coupled with an X-ray energy dispersive spectroscopy (EDS) system from EDAX Genesis. Double-sided copper adhesive tape and coated with a platinum film in 2 cycles of 20 mA for 2 min was used, to ensure adequate electrical conductivity.

2.7. Temperature-programmed oxidation (TPO)

TPO was carried out to investigate the formation of carbon on the catalysts during the DRM for 24 h of TOS. The amount of carbon deposited on the spent catalyst

was measured by using a quadrupole mass spectrometer (Pffeifer, Prisma Plus) coupled to the reaction system. After the reaction, the samples were cooled to room temperature in He and, subsequently, heated to 1173 K, under a 21% O_2: He mixture (70 mL.min^{-1}), with a heating rate of 10 K.min^{-1}. During this procedure, CO_2 was monitored by the mass spectrometer.

2.8. DRM reaction

The reaction was performed in a quartz reactor at 1073 K and atmospheric pressure using a CH_4/CO_2 molar ratio of 1. Prior to the reaction, the samples were diluted with SiC (SiC/catalyst ratio of 1.5) and then reduced under H_2 flow (30 mL.min^{-1}) at 1073 K for 1 h. The effluent gas of the reactor was analyzed using a gas chromatograph (Agilent 6890A), equipped with a thermal conductivity detector and a Carboxen 1010 column. The conversion of methane and CO_2 and the selectivity to products were calculated using the following equations:

$$X_i = \frac{(n_i)_{feed} - (n_i)_{exit}}{(n_i)_{feed}} \; x\,100 \qquad (2)$$

$$S_x = \frac{(n_x)_{produced}}{(nCH_4)_{feed}} \; x\,100 \qquad (3)$$

Where i = CH_4 or CO_2 and $(n_x)_{produced}$ = mols of x produced (x = H_2, CO)

3. Results and discussion

3.1. Catalyst characterization

Raman spectra of CeO_2 and Ni/CeO_2 samples calcined at different temperatures are shown in Fig. 1. The Raman spectra of the supports calcined at different temperatures (Fig. 1a) showed one band assigned to the symmetric stretching mode of the eight oxygen atoms around the Ce^{4+} cation characteristic of CeO_2 with fluorite structure [29-31]. In our work, this band is located at 463 cm^{-1} (CeO_2_673); 464 cm^{-1} (CeO_2_873); 465 cm^{-1} (CeO_2_1073); 465 cm^{-1} (CeO_2_1473). Decreasing calcination temperature decreased the intensity of this band that became broader and asymmetric on the low-energy side. These results are attributed to the decrease in ceria crystallite size that increases the lattice constant [32]. In the graphic inside Fig. 1a, it is possible to identify shoulders at 255 and 590 cm^{-1} for CeO_2_673 sample, which decreases in intensity as the calcination temperature increases. The band at 590 cm^{-1} has been attributed to the presence of oxygen vacancies defects created in the lattice of CeO_2 with small particle size (nanoparticles) [32] or by incorporating of cations into CeO_2 [33,34]. Spanier et al. [32] reported the Raman spectra from bulk ceria (5 μm) and ceria nanoparticles with different crystallite sizes (6.1 to 25 nm). The Raman spectrum of bulk ceria did not reveal the presence of this band but decreasing the crystallite size to 25 nm led to its appearance. Further decrease in the CeO_2 crystallite size significantly increased the intensity of this band. The decrease in the size of CeO_2 nanoparticles is accompanied by a significant increase in the lattice parameter, which is associated with the reduction of Ce^{4+} to Ce^{3+} due to a higher fraction of oxygen vacancies that can be accommodated on the high surface area per unit volume of smaller nanoparticles [32]. The band at 255 cm^{-1} is attributed to second-order transverse acoustic (2TA) mode of CeO_2 with lattice defects [35].

The Raman spectra of the catalysts is displayed in Fig. 1b. All catalysts exhibit the band corresponding to the F_{2g} Raman mode observed for the supports at around 463-465 cm^{-1}. However, the addition of Ni slightly shifted this band to lower frequency in comparison to the pure supports except for the sample calcined at 1473 K: 461 cm^{-1} (5Ni/CeO_2_673); 461 cm^{-1} (10Ni/CeO_2_673); 462 cm^{-1} (10Ni/CeO_2_873); 463 cm^{-1} (10Ni/CeO_2_1073); 465 cm^{-1} (10Ni/CeO_2_1473). In addition, the band around 550 cm^{-1} attributed to oxygen vacancies is more intense and broader with the appearance of shoulder at 625 cm^{-1} for all catalysts except for the sample calcined at 1473 K. In this case, oxygen vacancies defects were likely created by the formation of Ce^{3+} species due to the small ceria crystallite size as well as to the incorporation of Ni^{2+} into ceria lattice [33]. The replacement of Ce^{4+} by Ni^{2+} atoms lead to the reduction of Ce^{4+} to Ce^{3+} and the creation of oxygen vacancies to compensate the charge balance. This is the reason for the higher intensity of this band on the spectra of catalysts in comparison to the ones for the respective supports. The shoulder at 625 cm^{-1} was attributed to presence of Ce^{3+} or Ni^{3+} cations in the CeNi solid solution phase [36]. The spectra of the catalysts exhibit two bands at low Raman shift: 225 and 262 cm^{-1}. The new band observed at 225 cm^{-1} on the spectra of the samples calcined at 673, 873 and 1073 K is attributed to Ce–OH vibrations, which result from the surface defects created by the incorporation of Ni^{2+} into the ceria lattice [33].

(a)

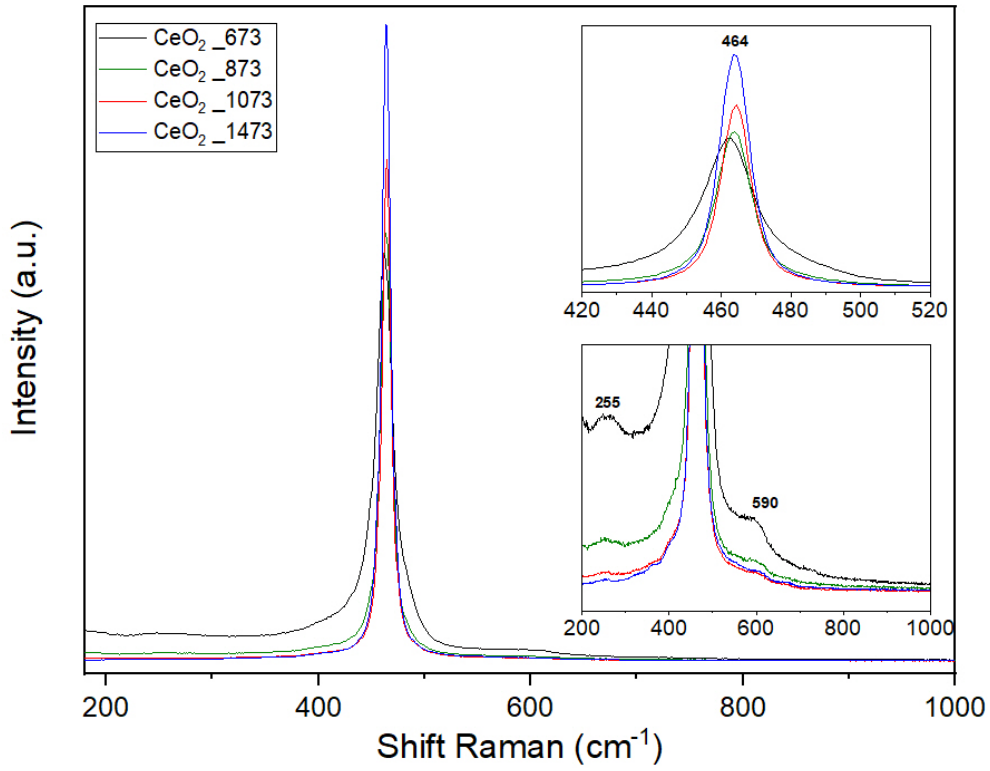

(b)

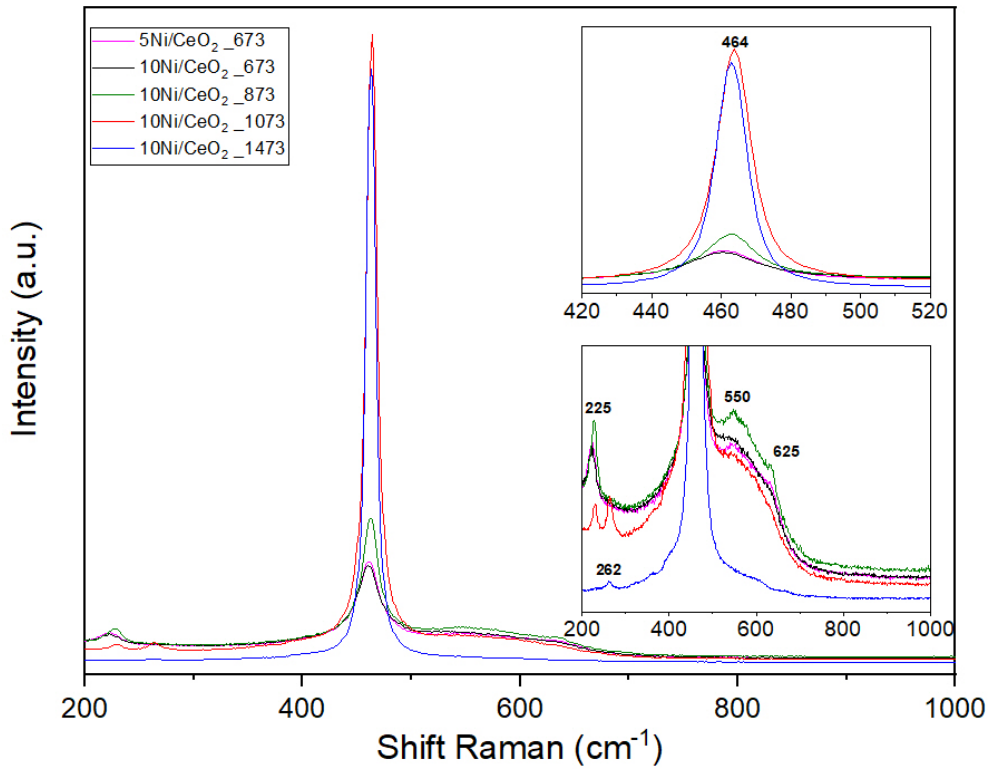

Figure 1 – Raman spectra for (a) supports and (b) catalysts calcined at different temperatures obtained from 200 to 1000 cm^{-1}. Insets provides expanded views of the band at 464 cm^{-1}.

Therefore, in our work, the Raman spectra suggest that Ni was partially incorporated into the ceria lattice, with the creation of oxygen vacancies mainly for the samples calcined at 673, 873 and 1073 K. This result has been also reported for the addition of different dopants to ceria [37-40].

Barrio et al. [39] investigated the structural and electronic properties of $Ce_{1-x}Ni_xO_{2-y}$ samples containing 10 and 20 wt% NiO. Raman spectra revealed a broadening and a strong shift of the band at 460 cm^{-1} for CeO_2 to 445 cm^{-1} for $Ce_{1-x}Ni_xO_{2-y}$ samples. These results were attributed to the formation of a solid solution with the insertion of Ni into the ceria structure. Yisup et al. [40] also observed the formation of a solid solution for $Ce_{1-x}Ni_xO_{2-y}$ samples. Raman spectra showed a shift of the band at 460 cm^{-1} for pure CeO_2 to lower frequencies for $Ce_{1-x}Ni_xO_{2-y}$ samples (440 cm^{-1}). In addition, it was also observed the appearance of well-defined bands at 213 and 564 cm^{-1}, which suggested the incorporation of Ni into ceria lattice and the creation of oxygen vacancies.

In situ XRD experiments were carried out during the reduction under pure hydrogen from room temperature to 1073 K for 10Ni/CeO_2_673, 10Ni/CeO_2_1073 and 10Ni/CeO_2_1473 samples and a physical mixture containing bulk NiO and CeO_2 (Fig. S1). The X-ray diffraction patterns obtained at selected temperatures are shown in Fig. 2. The diffractograms recorded between 2θ = 18.2 - 22.5 º and 2θ = 27.6 - 30.2 º are shown in Fig. S2 to better follow the evolution of ceria and metallic Ni/NiO phases as the reduction temperature increases.

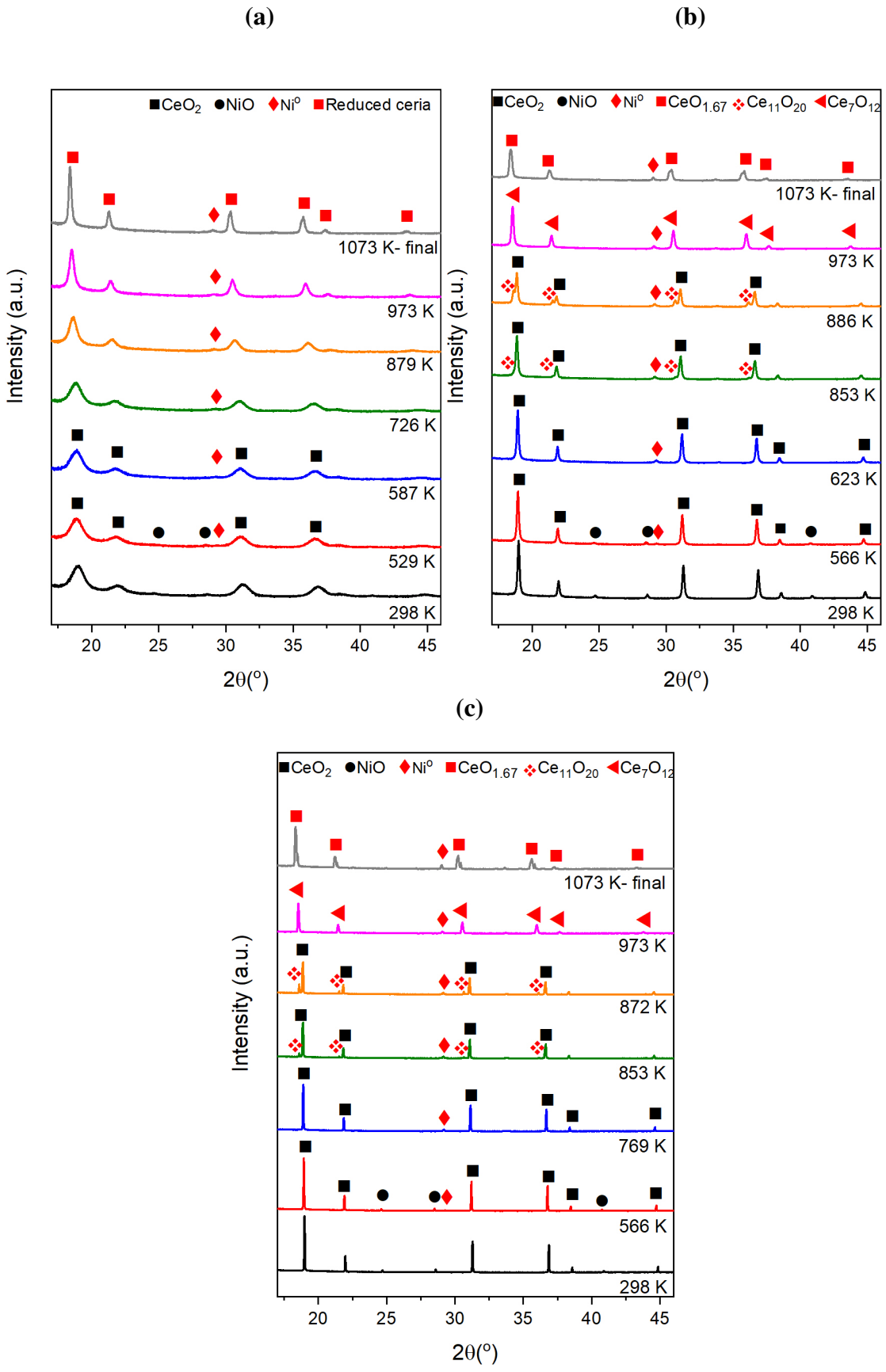

Figure 2 - X-ray diffraction patterns obtained for (a) 10Ni/CeO_2_673; (b) 10Ni/CeO_2_1073; (c) 10Ni/CeO_2_1473 at selected temperatures.

The diffractograms of the 10Ni/CeO_2_673 showed the displacement of the CeO_2 diffraction lines to lower values of 2θ as the reduction temperature increased. This shift in CeO_2 diffraction lines during reduction was also reported in the literature [13,26,39,41,42] and it was attributed to both the thermal expansion of the lattice and the conversion of Ce^{4+} to Ce^{3+} species with the creation of oxygen vacancies in the CeO_2 structure. Since the ionic radii of Ce^{3+} (1,03 Å) is larger than that one for Ce^{4+} (0,97 Å), the substitution causes the expansion of the lattice, which shifts the diffraction lines to lower values of 2θ.

Barrio et al. [39] attributed this shift to the reduction of a mixed oxide ($Ce_{1-x}Ni_xO_{2-y}$), involving the reduction of Ni^{2+} to Ni^0 and Ce^{4+} to Ce^{3+}. The formation of Ce^{3+} species was responsible for the expansion of the lattice. Recently, this $Ce_{1-x}Ni_xO_{2-y}$ phase was also detected by *in situ* XRD during DRM reaction [43]. In our work, Raman spectra of Ni/CeO_2 samples revealed the presence of $Ce_{1-x}Ni_xO_{2-y}$. Therefore, this shift on the ceria lines can be attributed to the reduction of Ce^{4+} present on ceria as well as on $Ce_{1-x}Ni_xO_{2-y}$ solid solution.

When the sample was heated to 529 K, it was also observed a decrease in the intensity of the characteristic lines of NiO and the appearance of the line corresponding to Ni^0, but this line was too broad to measure Ni^0 crystallite size. At 587 K, the NiO lines were no longer detected, suggesting that Ni was completely reduced at this temperature. The increase of temperature to 1073 K led to an increase in the intensity of the diffraction lines, suggesting a sintering of CeO_2 and Ni^0 particles.

10Ni/CeO_2_1073 and 10Ni/CeO_2_1473 samples and the physical mixture showed similar behavior of the sample calcined at 673 K during reduction. However, since these samples presented higher crystallinity, the phase transitions of CeO_2 during reduction were clearly observed. At 853 K, the diffractograms of these catalysts

exhibited the lines corresponding to the $Ce_{11}O_{20}$ phase with triclinic structure (ICSD-88758). Increasing temperature to 973 K, the characteristic lines of Ce_7O_{12} phase with rhombohedral structure were detected (ICSD-88755). At this temperature, the lines characteristic of CeO_2 phase were no longer detected. Finally, the $CeO_{1.67}$ phase with bixbyite structure (ICSD-88753) was observed at 1073 K. Therefore, the following ceria phase transitions were observed: $CeO_2 \rightarrow Ce_{11}O_{20} \rightarrow Ce_7O_{12} \rightarrow CeO_{1.67}$.

The presence of these phases during reduction of CeO_2 was also reported by Bekheet et al [44]. According to the literature [44-46], the reduction of ceria leads to the formation of oxygen vacancies in a disordered manner, distorting the structure. Then, the increase of the disorder in the lattice results in the formation of new phases. Although the lines characteristic of these phases was not observed on the diffractograms during the reduction of 10Ni/CeO_2_673, their presence cannot be ruled out. The sample calcined at 673 K exhibited low crystallinity, which makes more difficult to distinguish these different phases.

Regarding the Ni species, the appearance of the metallic Ni lines was detected at 566 K for the 10Ni/CeO_2_1073 and 10Ni/CeO_2_1473 samples and physical mixture. The NiO lines were no longer observed at 623 K (for 10Ni/CeO_2_1073) and 769 K (for 10Ni/CeO_2_1473 and physical mixture). Comparing these results with those obtained for the sample calcined at 673 K, it was observed that increasing calcination temperature decreased the reducibility of NiO crystallites, which according to the literature [47] is related to the increase of Ni particles size. As the calcination temperature rises, the crystallite size of the NiO increases, requiring higher reduction temperatures.

Fig. 3 shows the variation of NiO and Ni^0 crystallite size of Ni/CeO_2 catalysts as a function of reduction temperature. All catalysts exhibited an increase of the Ni^0

crystallite size as the reduction temperature was increased to 1073 K but the degree of crystallite growth depended on the calcination temperature. For 10Ni/CeO_2_673, the Ni^0 crystallite increased from 10 to 20 nm. Ni^0 crystallite size grew from 20 to 46 nm for the sample calcined at 1073 K and the larger increase was observed for the sample calcined at 1473 K (27 to 116 nm). Marinho et al. [13] also reported a significant growth in the metallic Ni crystallite size from 5 to 33 nm during the reduction at 1073 K of a 10Ni/CeO_2 catalyst prepared by incipient wetness impregnation and calcined at 673 K. This result was attributed to the sintering of ceria during reduction.

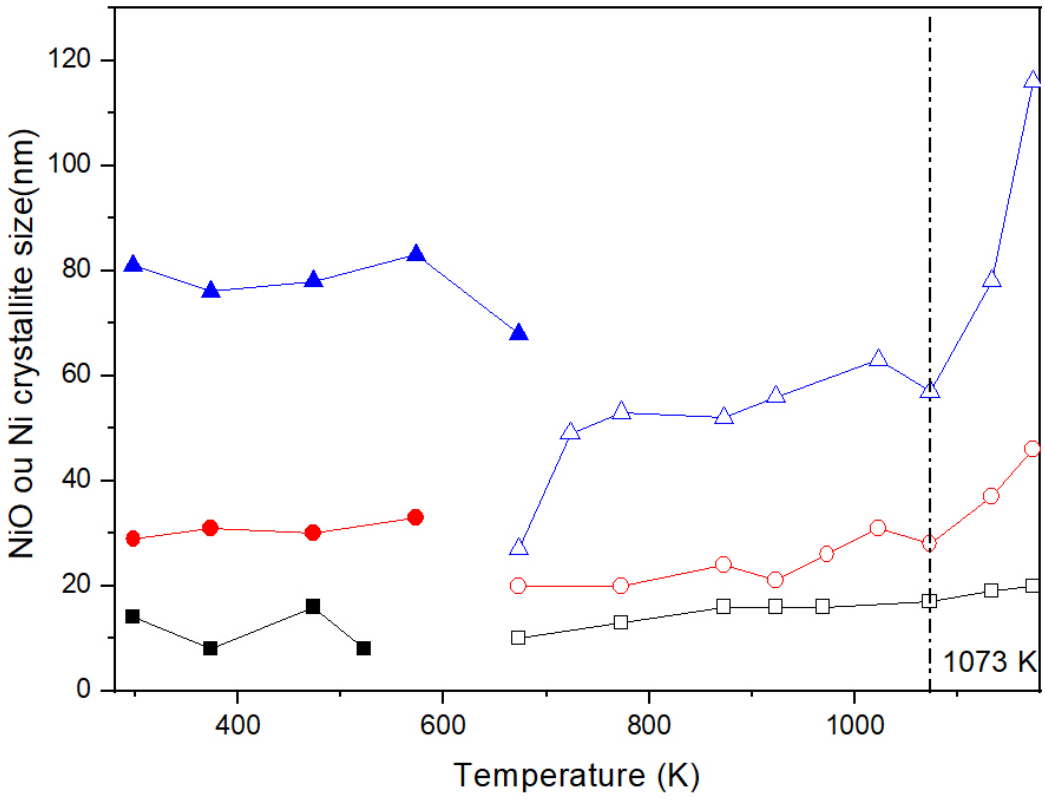

Figure 3 – Evolution of NiO and Ni^o crystallite size during reduction of the catalysts. 10Ni/CeO_2_673: (■) NiO; (□) Ni^o; 10Ni/CeO_2_1073: (●) NiO; (○) Ni^o; 10Ni/CeO_2_1473: (▲) NiO; (△) Ni^o.

Table 1 lists the Ni^0 crystallite size calculated from the diffractograms obtained after reduction of Ni/CeO_2 catalysts at 1073 K. The diffractograms of 5Ni/CeO_2_673

and 10Ni/CeO_2_873 catalysts after reduction at 1073 K and passivation are shown in Fig. S3. 5Ni/CeO_2_673 catalyst has the smallest Ni^0 crystallite size (10 nm), whereas it is two-fold larger for the catalyst containing 10 wt. % of Ni and calcined at the same temperature (20 nm). Increasing the calcination temperature significantly increased the Ni^0 crystallite size from 20 to 116 nm.

The reduction of ceria and NiO was also monitored by XANES analyses for 10Ni/CeO_2_673, 10Ni/CeO_2_1073 and 10Ni/CeO_2_1473 samples. The measurements were made at the L_{III}-edge of the ceria and at the K-edge of the nickel under a mixture containing 5% H_2/He from room temperature to 1073 K. The XANES spectra at the L_{III}-edge of ceria during reduction of the samples and DRM reaction are shown in Figs. S4 and 4.

Fig. S4 shows the spectra of 10Ni/CeO_2 calcined at 673, 1073 and 1473 K during reduction and DRM at 1073 K. At 298 K, the spectra exhibited two peaks around 5731 and 5738 eV, characteristic of Ce^{4+} species. With the increase in the temperature, the intensities of these peaks decreased and a new peak appeared at 5728 eV, indicating the reduction of ceria.

The ceria reduction is followed in more detail in Fig. 4 that shows the spectra of references (CeO_2 and $Ce(CH_3CO_2)_3$) and Ni/CeO_2 samples at selected reduction temperatures. The spectrum of CeO_2 exhibited two absorption peaks at 5732 eV (peak B) and 5739 eV (peak C) corresponding to the Ce^{4+} species (Fig. 4a). The peak B is assigned to the transition of an electron from the oxygen 2p orbital to the 4f orbital of the Ce atom, as well as to the transition of an electron from the 2p orbital of Ce to the 5d orbital. The peak C corresponds to the absorption into the 5d orbital of Ce while 4f orbital is empty. For the spectrum of $Ce(CH_3CO_2)_3$ reference that is characteristic of the

Ce^{3+} species, a band at 5728 eV (peak B_0) was observed. This is related to the electronic transitions into the 5d orbitals with 4f orbital occupied [48-51].

Table 1- Crystallite size of Ni^0 calculated through X-ray diffraction after reduction at 1073 K and the rate of carbon deposition during the DRM at 1073 K for 24h TOS for this work and from the literature.

Catalyst	Reactions Conditions	Ni^0 crystallite size (nm)	mgC/(g_{cat}.h)	Reference
5%Ni/CeO_2_673*	1073 K, CH_4:CO_2= 1	10	1.6	Our work
10%Ni/CeO_2_673	1073 K, CH_4:CO_2= 1	20	20.9	Our work
10%Ni/CeO_2_873*	1073 K, CH_4:CO_2= 1	28	10.6	Our work
10%Ni/CeO_2_1073	1073 K, CH_4:CO_2= 1	46	5.9	Our work
10%Ni/CeO_2_1473	1073 K, CH_4:CO_2= 1	116	0.3	Our work
10%Ni/CeO_2	1073 K, CH_4:CO_2= 1	33	9.7	[13]
10%Ni@CeO_2	1073 K, CH_4:CO_2= 1	19	1.6	[13]
Ni/CeO_2	1073 K, CH_4:CO_2= 1	24	4.8	[20]
$LaNiO_3$	1073 K, CH_4:CO_2= 1	46	27.0	[18]
$LaNiO_3$/Al_2O_3	1073 K, CH_4:CO_2= 1	41	7.6	[18]
$LaNiO_3$/$CeSiO_2$	1073 K, CH_4:CO_2= 1	28	0.3	[18]
5%Ni-CeAl	1073 K, CH_4:CO_2= 1	5	0.0	[15]
10%Ni-CeAl	1073 K, CH_4:CO_2= 1	4	0.0	[15]
10%Ni/CeAl	1073 K, CH_4:CO_2= 1	11	2.0	[15]
3%Ni/CeO_2-TiO_2	1023 K, CH_4:CO_2= 1	22	0.2	[65]
7.5%Ni/CeO_2-TiO_2	1023 K, CH_4:CO_2= 1	32	4.6	[65]
10%Ni/CeO_2-TiO_2	1023 K, CH_4:CO_2= 1	45	5.1	[65]
18Ni/CeNb	1073 K, CH_4:CO_2= 1	32	6.5	[24]
18Ni/CeZr	1073 K, CH_4:CO_2= 1	24	9.7	[24]

*Crystallite size of Ni^o was calculated after reduction and passivation of samples.

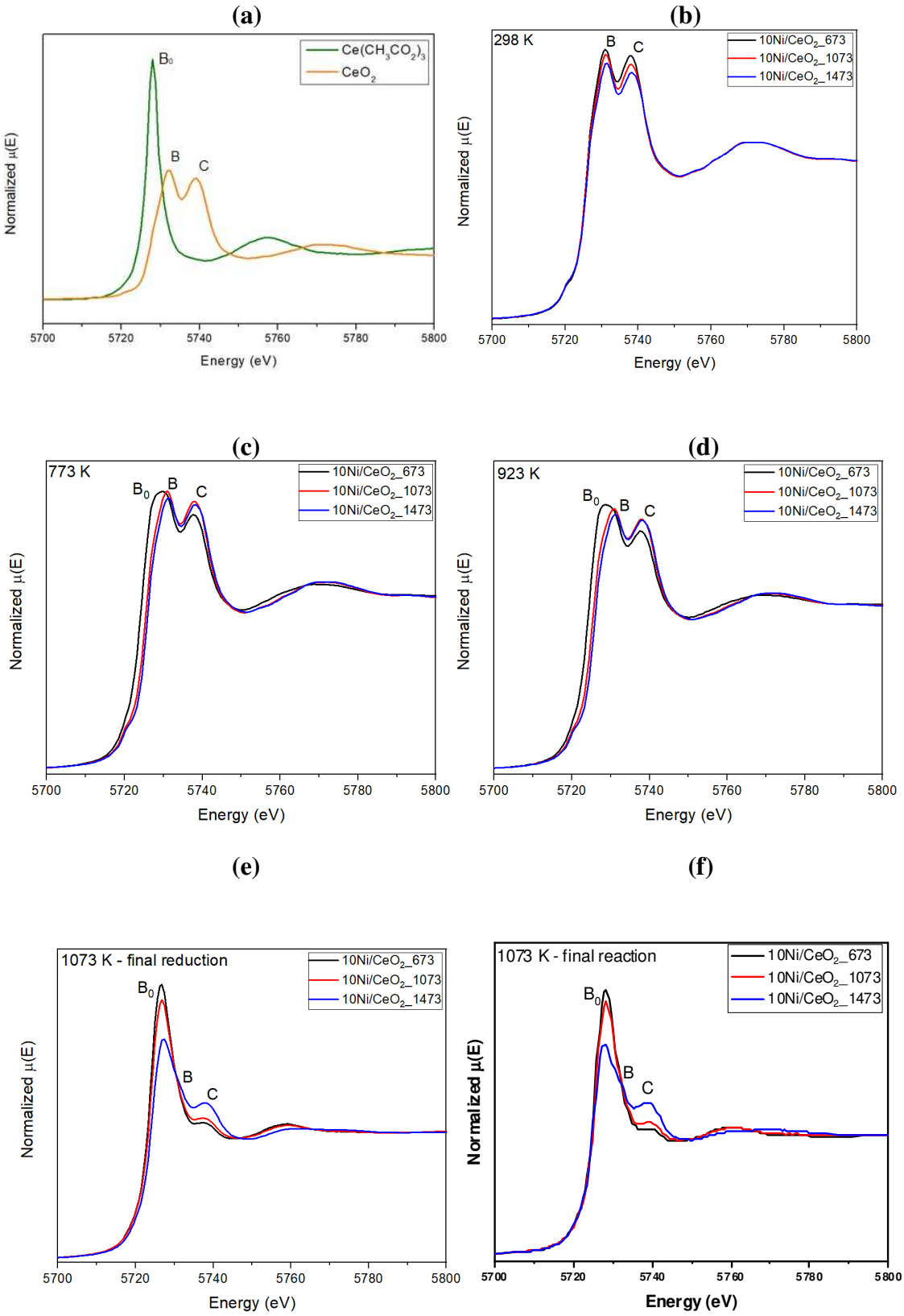

Figure 4 – *in situ* XANES spectra at Ce L_{III} - edge of references ($Ce(CH_3CO_2)_3$ and CeO_2) and catalysts after reduction at selected temperatures: (b) 298 K; (c) 773 K; (d) 923 K; (e) 1073 K; and (f) after DRM at 1073 K.

The XANES spectra of all samples at 298 K showed the peaks B and C, indicating the presence of Ce^{4+} species (Fig. 4b). After reduction at 773 K, the peak B_0 was also observed for the sample 10Ni/CeO_2_673 (Fig. 4c). For the samples calcined at 1073 and 1473 K, a shoulder was detected in this region. These results reveal the reduction of Ce^{4+} to Ce^{3+}, which was more significant for 10Ni/CeO_2_673 catalyst. Increasing the reduction temperature to 923 K slightly increased the intensity of the peak B_0 for all catalysts (Fig. 4d). At 1073 K, a strong change in the spectra of all samples was observed, indicating the presence of a higher amount of Ce^{3+} species (Fig. 4e). After DRM reaction at 1073 K, the spectra of all catalysts remained unchanged (Fig. 4f).

Fig. S5 shows the evolution of the fraction of Ce^{4+} and Ce^{3+} species during reduction at different temperatures, calculated by the linear combination of Ce L_{III} edge XANES spectra of Ce^{4+} and Ce^{3+} references. For 10Ni/CeO_2_673 catalyst, the reduction of Ce^{4+} to Ce^{3+} started at around 450 K and leveled off at 600 K. In the temperature range between 600 and 1000 K no significant change in the fraction of Ce^{4+} and Ce^{3+} species was observed. However, above 1000 K, an increase in reduction of Ce^{4+} to Ce^{3+} was detected. The same behavior was observed for Ni/CeO_2_1073 with the reduction starting at 450 K and levelling off at 700K and increasing again at 900K. For the catalyst calcined at 1473 K, the reduction was observed only at 1000 K. According to the literature [52-54], the reduction of ceria takes place into two regions: (i) the low temperature region, which corresponds to the reduction of the surface ceria and (ii) the high temperature region that is related to the reduction of bulk ceria. Thus, in this work, the reduction at low temperatures (450-900 K) can be attributed to the reduction of surface CeO_2, while the reduction above 900 K (high temperature) can be associated with the reduction of bulk CeO_2. The contribution of each temperature region depends

on the surface area of CeO_2 [52]. Therefore, the higher reducibility of the sample calcined at 673 K can be attributed to its higher surface area, which leads to the presence of a larger amount of surface ceria. On the other hand, for the sample calcined at 1473 K, only the bulk cerium oxide was present due to its low surface area. Then, the reduction occurs only at high temperatures. Fig. S5 also shows the fraction of Ce^{4+} and Ce^{3+} species during DRM reaction at 1073 K for 1h. The fraction of Ce^{4+} and Ce^{3+} species after reduction and reaction remained approximately constant, indicating that no oxidation of the support was observed in the presence of the feed containing CO_2.

Table 2 lists the fraction of Ce^{3+} species obtained for all catalysts after reduction at 1073 K and DRM reaction at 1073 K. The sample calcined at lower temperature exhibited the highest fraction of Ce^{3+} species (56%). The increase in the calcination temperature led to a decrease in the fraction of Ce^{3+} species, which was 48 and 38 % for 10Ni/CeO_2_1073 and 10Ni/CeO_2_1473 catalysts, respectively. Taking into account the results presented above, it can be concluded that increasing calcination temperature decreased the reducibility of CeO_2. However, the fraction of Ce^{3+} species remained approximately unchanged during the reaction.

Table 2- Ce^{3+} molar fraction calculated by the linear combination of Ce L_{III}-edge XANES spectra of the catalysts.

Catalysts	Ce^{+3} molar fraction (%)	
	Reduction	Reaction
10Ni/CeO_2_673	56	58
10Ni/CeO_2_1073	48	50
10Ni/CeO_2_1473	38	38

Fig. S6 shows XANES spectra at the Ni K-edge during reduction of the 10Ni/CeO_2 samples calcined at 673, 873 and 1073 K. The XANES spectra at the Ni K-edge of references (NiO and Ni foil) and after reduction of 10Ni/CeO_2_673, 10Ni/CeO_2_1073 and 10Ni/CeO_2_1473 catalysts at selected temperatures are shown in Fig. 5.

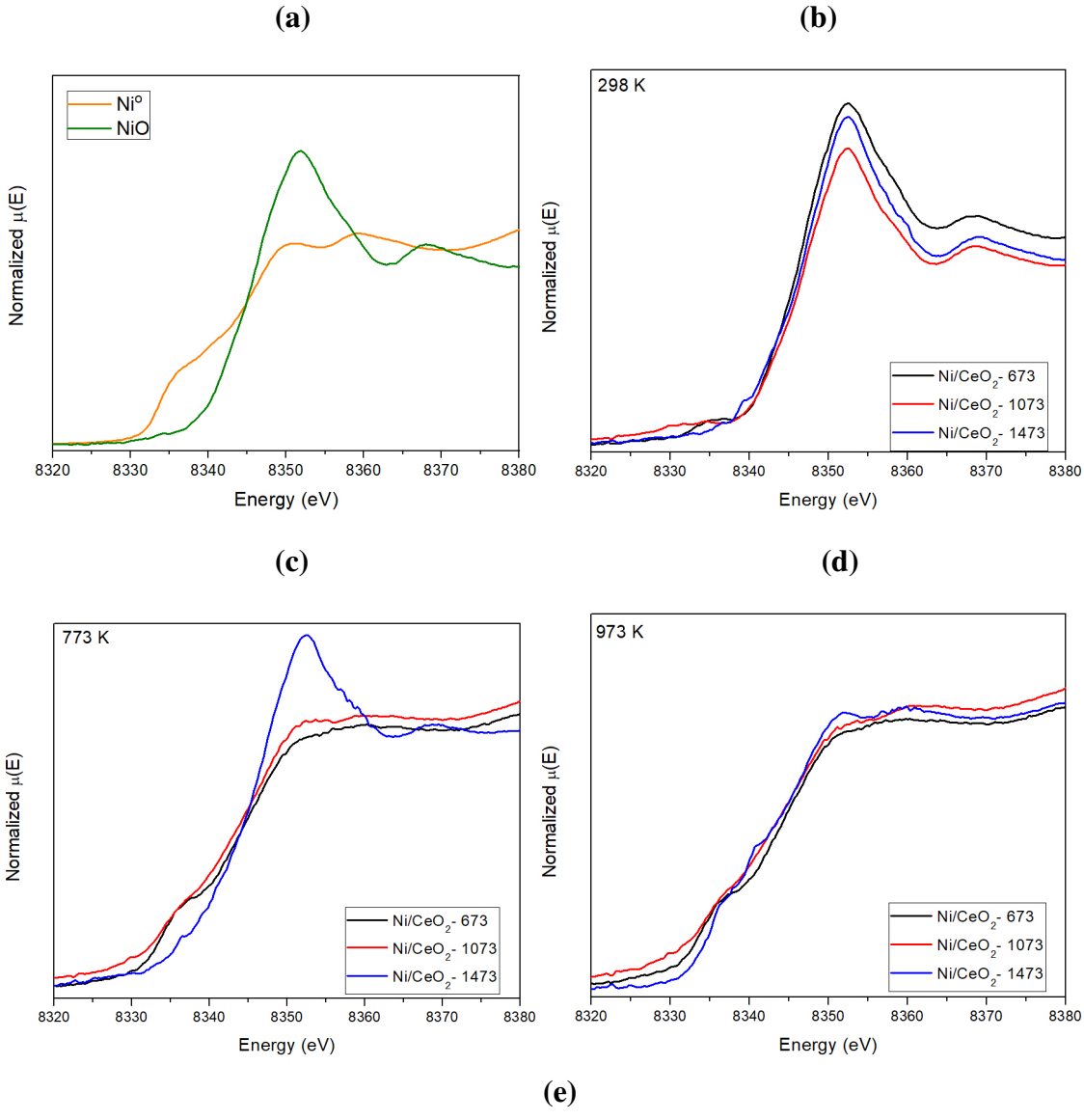

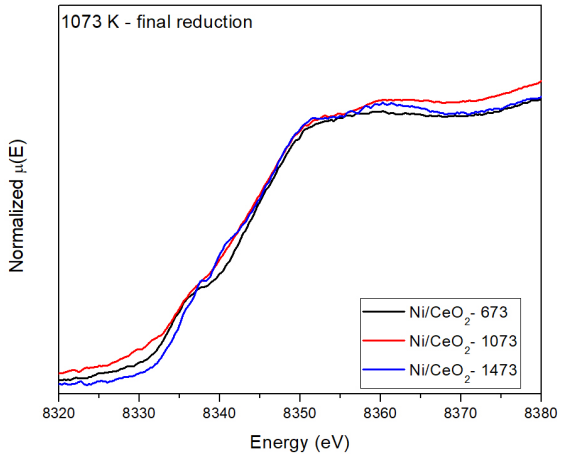

Figure 5 – *in situ* XANES spectra at the Ni K-edge of (a) references (NiO and Ni foil) and after reduction of 10Ni/CeO_2_673, 10Ni/CeO_2_1073 and 10Ni/CeO_2_1473 catalysts at selected temperatures: (b) 298 K; (c) 773 K; (d) 973 K; (e) 1073 K.

At room temperature (Fig. 5b), the spectra obtained for all 10Ni/CeO_2 samples exhibited a peak at 8352 eV characteristic of NiO. As the reduction temperature increased, the intensity of this peak decreased, indicating the reduction of Ni^{2+} species to Ni^0. After reduction at 773 K (Fig. 5c), the spectra of the 10Ni/CeO_2_673 and 10Ni/CeO_2_1073 samples are similar to that of the metallic Ni foil, indicating the complete reduction of NiO at this temperature. The spectrum of the 10Ni/CeO_2_1473 sample did not change significantly, suggesting the presence of Ni^{2+} species yet. A strong change in the spectra of 10Ni/CeO_2_1473 sample was observed after reduction at 973 K, indicating the occurrence of the reduction of nickel oxide (Fig. 5d). However, the presence of Ni^{2+} species can still be detected. Spectra of all samples reduced to 1073 K show complete reduction of Ni oxide (Fig. 5e).

In order to evaluate the degree of NiO reduction as a function of temperature, the linear combination between the XANES spectra of the samples and the NiO and metallic Ni foil spectra was performed (Fig. S7).

The results obtained showed that the calcination temperature affected the initial reduction temperature of NiO. The reduction of NiO began at 320, 480 and 570 K, for

10Ni/CeO_2_673, 10Ni/CeO_2_1073 and 10Ni/CeO_2_1473 catalysts. The temperature necessary for the complete reduction of NiO was 750 K (for 10Ni/CeO_2_673); 800 K (10Ni/CeO_2_1073) and 1000 K (10Ni/CeO_2_1473). These results revealed that the kinetic for the reduction of large NiO particles is slower than that for small particles [55,56]. Gonzalez-Dela Cruz et al [57] also observed that NiO was only completely reduced at high temperature (823 K) for 26 wt.% Ni/CeO_2 catalyst calcined at 1023 K, using XANES analyses at the K-edge of Ni.

Thus, in the present work, the XANES results are in agreement with the *in situ* XRD analyses and confirm that increasing calcination temperature increased the temperature required for complete nickel oxide reduction.

Furthermore, the reduction of NiO affected the reduction of ceria, which depends on the metallic Ni crystallite size. Fig. S8 shows the evolution of Ni and Ce species fraction as a function of reduction temperature. For 10Ni/CeO_2_673 and 10Ni/CeO_2_1073 samples, the reduction of NiO is accompanied by the reduction of surface ceria. These results suggests that after the formation of metallic Ni particles, hydrogen is activated on the Ni surface and by spillover it migrates to the support, which promotes the reduction of ceria located on the surface. On the other hand, this mechanism does not take place on the catalyst calcined at higher temperature. For the 10Ni/CeO_2_1473, surface ceria is not reduced that is likely due to the low contact between the large Ni^0 crystallites and the support as well as the low surface area of the catalyst. The reduction of bulk ceria occurs at the same temperature for all catalysts (above 900 K), regardless the Ni crystallite size.

3.2 Catalytic tests

The methane and CO_2 conversions and the H_2/CO molar ratio as a function of time on stream (TOS) obtained for the CO_2 reforming of CH_4 at 1073 K are shown in Fig. 6. The catalysts exhibited initial methane and CO_2 conversions around 57-71 and 68-79%, respectively. 5Ni/CeO_2_673 and the catalysts containing 10 wt% Ni calcined at 673, 873 and 1073 K slightly deactivated during TOS, whereas 10Ni/CeO_2_1473 catalyst underwent a more significant drop in CH_4 and CO_2 conversions at the beginning of reaction. A bulk NiO catalyst was also tested as reference and the result obtained was similar to the one for 10Ni/CeO_2_1473 catalyst.

Regarding the selectivity to products, H_2, CO and H_2O were detected for all catalysts. Furthermore, the values of initial H_2/CO molar ratios were between 0.94-0.81 for all catalysts and remained constant during 24 h of TOS. H_2/CO molar ratio values lower than 1.0, CO_2 conversion higher than CH_4 conversion, and water formation indicate the occurrence of the reverse water gas shift reaction, as reported in the literature [58-60].

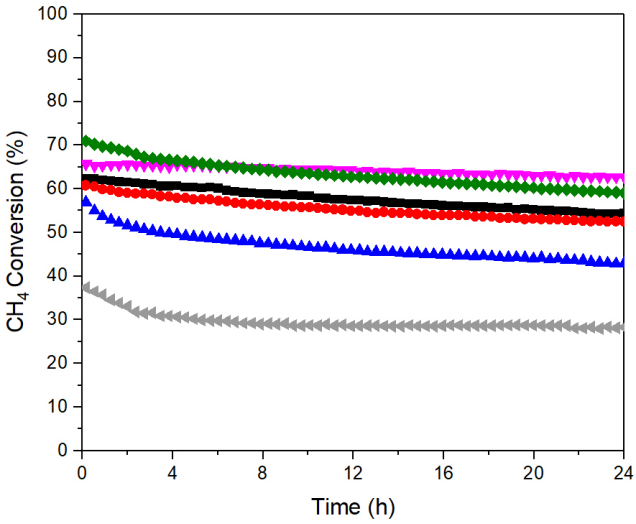

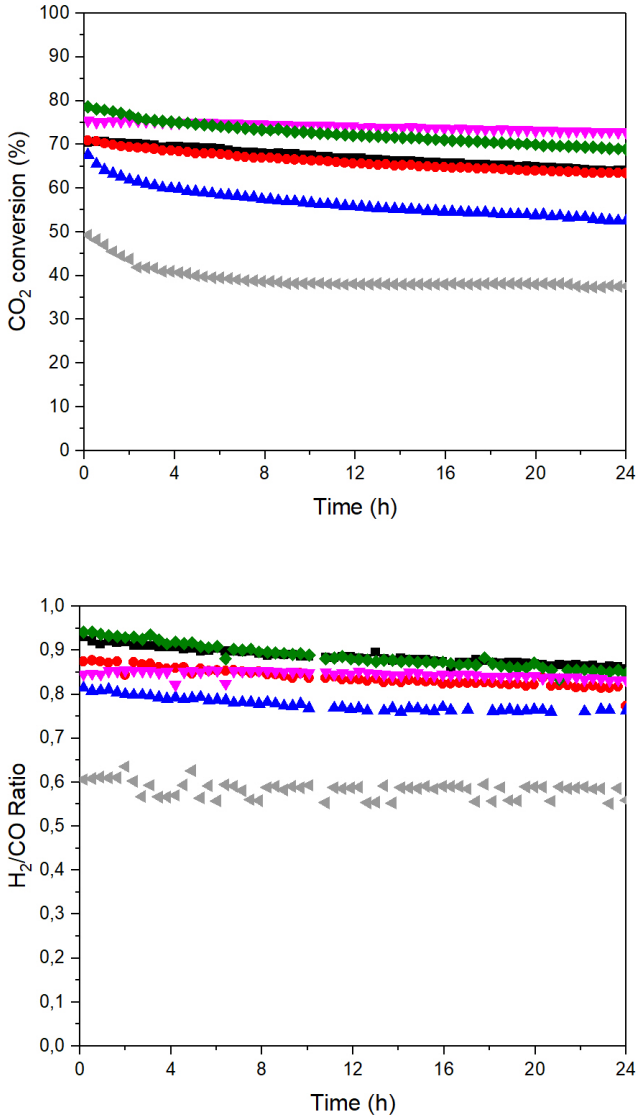

Figure 6 – Methane and CO_2 conversion and H_2/CO ratio versus TOS for CO_2 reforming of methane at 1073K for the catalysts: (▼) 5Ni/CeO_2_673; (■) 10Ni/CeO_2_673; (◆)10Ni/CeO_2_873; (●)Ni/CeO_2_1073; (▲)Ni/CeO_2_1473; (◀) NiO.

Since one of the main causes of deactivation of the catalysts on dry reforming of methane is related to carbon deposition, the catalysts were characterized after reaction for 24 h of TOS using scanning electron microscopy (SEM) and programmed oxidation temperature (TPO) to investigate the formation of carbon deposits.

Fig. 7 presents SEM images of catalysts calcined at different temperatures after dry reforming of methane. The results obtained showed the presence of carbon

filaments for the samples calcined at the 673 K and 1073 K. However, no carbon filaments were detected for the sample calcined at 1473 K.

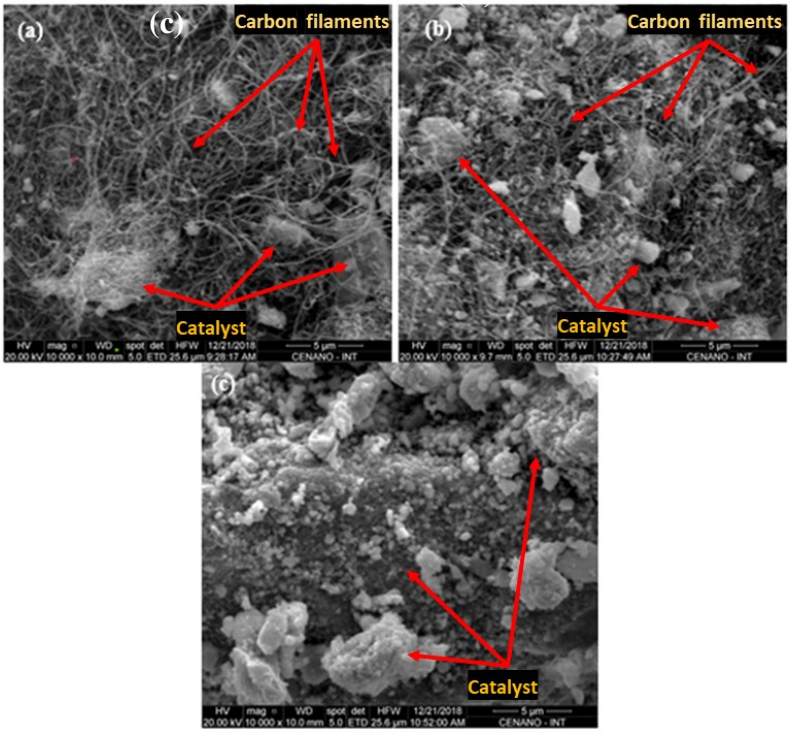

Figure 7 – SEM images of catalysts after DRM at 1073 K for 24 h: (a) 10Ni/CeO_2_673; (b) 10Ni/CeO_2_1073; (c) 10Ni/CeO_2_1473.

According to the literature [11,61-63], the formation of carbon filaments occurs by the decomposition of methane over metallic Ni crystallites. This carbon diffuses through the metal particle and the accumulation of carbon on the Ni particle leads to filament growth. Since the Ni particle is at the top of the filament, the catalyst remains active during the reaction. Thus, although carbon filaments were detected on samples calcined at 673 and 1073 K, no significant deactivation was observed during TOS.

The TPO profiles obtained for the Ni/CeO_2 catalysts and bulk NiO after DRM for 24 h of TOS are shown in Fig. S9. TPO profiles of 10Ni/CeO_2 catalysts calcined at

673, 873 and 1073 K showed intense peaks of CO_2 at around 902 - 912 K. From the graphic inside Fig. S9, it is also possible to notice peaks of CO_2 with low intensity around 865-951 K for 5Ni/CeO_2_673, 10Ni/CeO_2_1473 and bulk NiO. The 5Ni/CeO_2_673 and 10Ni/CeO_2_673 catalysts also exhibited a peak and a shoulder at around 724 K, respectively. The peaks in the TPO profile of spent catalysts after DRM have been attributed to the oxidation of different types of carbon: amorphous carbon, carbon filaments and graphite [64]. The characteristic temperature range for the oxidation of each type of carbon structure varies widely in the literature depending on the reaction and TPO experimental conditions used. Therefore, TPO analyses of well-defined carbonaceous structures (amorphous carbon, multi-wall carbon nanotube - MWNT, graphite) were performed to make the assignment of TPO peaks. The TPO profiles of these references are shown in Fig. S10. For the amorphous carbon, an oxygen uptake is observed between 623 and 823 K with a peak at 811 K. The TPO profile of MWCNT exhibited a peak at 873 K, whereas the oxidation of graphite takes place at high temperature (above 923 K). Then, the TPO profile of our spent catalysts revealed the presence of CO_2 formation below 823 K (5Ni/CeO_2_673 and 10Ni/CeO_2_673) attributed to oxidation of amorphous carbon, peaks between 823 - 923K associated with the oxidation of carbon filaments and oxidation of graphite above 923 K [13,18,64]. The formation of carbon filaments is in agreement with SEM images. Graphite was the main carbon species formed over bulk NiO.

Recently, Damaskinos et al. [65] reported a strong relationship between the Ni particle size and the type of carbon formed for DRM over Ni supported on CeO_2-TiO_2. Amorphous carbon was preferentially formed on the surface of small Ni particles, whereas carbon nanotubes were mainly produced on large Ni particles. The same result was observed in our work. Both catalysts calcined at 673 K with smaller Ni particle size

showed the formation of amorphous carbon on the surface of Ni particles. Ni/CeO_2 catalysts with Ni particle size larger than 10 nm exhibited mainly the formation of carbon nanotubes but graphite was also observed in minor amount in our work.

From the TPO profiles, the carbon formation rate during the DRM reaction was calculated and the values are presented in Table 1. The carbon deposition rate was lower over 5Ni/CeO_2_673, 10Ni/CeO_2_1473 and NiO, while the higher quantity of carbon formed was detected for 10Ni/CeO_2_673. Then, the carbon formation rate ($mg_C/(g_{cat}.h)$) followed the order: 10Ni/CeO_2_673 (20.9) > 10Ni/CeO_2_873 (10.6) > 10Ni/CeO_2_1073 (5.9) > 5Ni/CeO_2_673 (1.6) > 10Ni/CeO_2_1473 (0.3) ≈ NiO (0.2).

Table 1 also reports carbon formation rates for the DRM over different ceria-supported Ni catalysts from the literature [13,15,18,20,24,65]. The Ni crystallite size of the catalysts is also listed for comparison. There are several studies in the literature that report the amount of carbon formed during DRM over different catalysts and reaction conditions [13,15,18,20,24,65]. However, only few works describe the dependency of Ni crystallite size and the carbon formation rate for DRM over Ni-based catalysts. Supported $LaNiO_3$ derived catalysts [18] and Ni embedded on ceria-based supports [13] showed a continuous increase in the carbon formation rate as the Ni crystallite size increased (28 to 46 nm and 19 to 33 nm, respectively) after DRM at 1073 K. Damaskinos et al. [65] measured the rate of carbon formation for Ni/CeO_2-TiO_2 catalysts with different Ni content (3, 7.5 and 10 wt.%) after DRM at 1023 K during 12 h. The carbon formation rate sharply increased when the Ni particle size increased from 26.2 nm to 33.2 nm and thus, it leveled off for Ni particle size of 50 nm. Therefore, the relationship between carbon formation rate versus Ni crystallite size depends on the catalysts composition and preparation synthesis and reaction conditions.

According to the mechanism proposed in the literature for the carbon formation on hydrocarbon reforming reactions [11,61-63], initially, highly reactive carbon species (C_α) are produced from the dissociation of methane on the metallic nickel surface. C_α species can undergo gasification, forming CO. However, if the gasification rate is low or if excess of C_α species is formed, carbon may polymerize, generating C_β species. These species are less reactive and may lead to the occurrence of: (i) particle encapsulation, causing catalyst deactivation, or (ii) carbon filaments formation, which occurs through the dissolution of C_β species into nickel particles. The formation of carbon filaments does not cause an immediate deactivation of the catalyst as the metal particle surface remains free for reaction. In this mechanism, the size of nickel particles plays an important role on nucleation and growth of carbon filaments. The initiation step for carbon formation is more difficult for smaller particle sizes. There is a critical ensemble size, required for the carbon formation. Steam reforming requires ensembles of 3–4 atoms, whereas carbon formation needs 6–7 atoms. Therefore, it would be necessary to keep the size of Ni crystallites smaller than this critical size to avoid carbon formation [11]. The presence of large Ni crystallites would favor the growth of carbon filaments and carbon deposition. Vogt et al. [66] also reported a structure sensitivity for the formation of carbon deposits over silica supported Ni catalysts for DRM at 873 K. Increasing the Ni particle size from 1.2 to 6.0 nm increased the rate of carbon formation. They proposed that the formation of carbon occurs faster on the large particles containing highly coordinated sites. Bengaard et al. [67] also found that decreasing the Ni crystallite size decreases the rate of carbon formation and increases the initial temperature of carbon formation. Therefore, the support strongly influences the onset of carbon accumulation and this will happen faster on supports with low interaction with metal particle such as silica.

Fig. 8 shows the variation of carbon formation rate over Ni/CeO_2 catalysts for DRM during 24 h of TOS as a function of crystallite size of metallic Ni in this work. The rate of carbon formation increased as Ni crystallite size increased, achieving a maximum at around 20-30 nm and then, it continuously decreased up to 133 nm. Therefore, there is a critical Ni crystallite size for the formation of carbon during DRM reaction over Ni/CeO_2 catalysts, in which the maximum amount of carbon is formed.

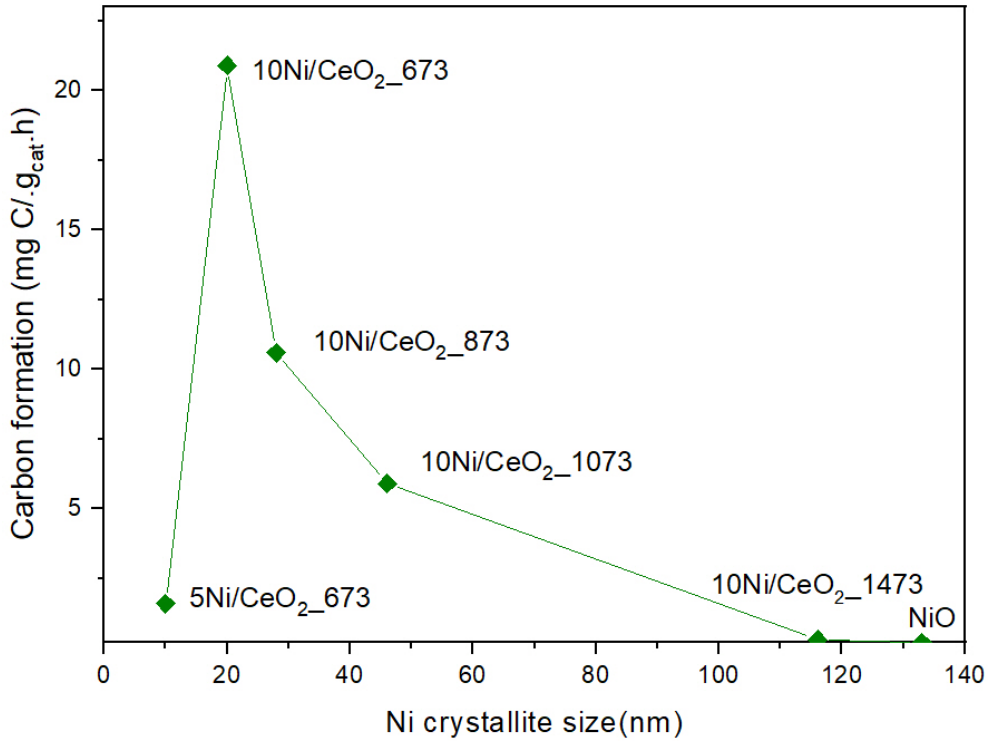

Figure 8- Carbon formation rate for DRM during 24 h of TOS as a function of Ni crystallite size after reduction at 1073 K for 1h.

The same results have been reported for the reaction of decomposition of methane for the production of carbon nanotubes and hydrogen [68-70]. Chen. et al. [70] studied the performance of Ni catalysts supported on hydrotalcites, $CaAl_2O_4$ and α-Al_2O_3 for methane decomposition reaction. They observed that carbon formation is favored when the size of the metal particles is between 20 and 40 nm. According to

them, the optimum Ni crystallite size for carbon filament formation is 34 nm. They also concluded that carbon deposition is inhibited for Ni particles smaller than 10 nm and for very large particles (220 nm). Toebes et al. [71] also did not detect the formation of carbon during methane decomposition over bulk NiO. According to them, the carbon filament growth is related to the balance between rates of methane dissociation and diffusion through the metal particle and the rate of nucleation and formation of the graphite layers. The unbalance between these rates inhibits the filament growth. Thus, carbon filament formation is only possible when all these steps are in equilibrium.

Our results obtained for DRM agrees very well with those for the decomposition of methane reaction. In fact, the decomposition of methane is the first step on the mechanism of CO_2 reforming of methane reaction. Damaskinos et al. [65] suggested that methane decomposition is the main reaction pathway for carbon deposition as the Ni particle size increased from 22 to 45 nm over Ni/CeO_2-TiO_2 catalysts.

Fig. 8 reveals the existence of a window for carbon formation during the DRM: below 10 nm and above 100 nm carbon deposition is negligible. In general, the few works that investigate the effect of Ni particle size on carbon formation rate for DRM [8,13,65,66] do not evaluate the performance of catalysts with very large Ni particle size (above 100 nm), which is typical of the anodes for SOFC [72]. The results of our work demonstrate that Ni-based SOFC anodes may operate with very low carbon deposition during DRM since very large Ni particles are formed during anode synthesis and reduction.

Furthermore, a support with redox properties such as ceria, often plays a key role on the DRM reaction. The highly reactive carbon species (C_α) formed may reacts with oxygen from the support producing CO and creating oxygen vacancies [13,17,18]. The oxygen vacancies are replenished by the dissociative adsorption of CO_2 on the support.

Therefore, the support participates on the mechanism of carbon removal, keeping the metal surface free of carbon deposits. The unbalance between the methane decomposition rate and the reaction rate of carbon with oxygen from the support will lead to the accumulation of a less active carbon (C_β) that may also migrate into the nickel particle producing carbon filaments. However, the effectiveness of the carbon removal mechanism also depends on the metal-support interaction and thus, on the metal particle size. A higher metal-support interface favors the oxygen migration from the support to the metal surface and then, suppress or reduces the accumulation of carbon. Therefore, this mechanism is promoted on highly dispersed metal particles over supports with redox properties such as ceria or ceria-zirconia mixed oxides. Vogt et al. [66] also pointed out that the size of metal nanoparticles affects the metal-support interaction and, consequently, different growth mechanisms for carbon nanotubes may take place.

Therefore, the higher amount of oxygen vacancies of the ceria support calcined at 673 K and the smaller Ni crystallite size on the 5Ni/CeO_2_673 catalyst leads to a lower carbon formation rate. Increasing the Ni crystallite size to 20 nm reduces the metal-support interface and increases the carbon formation rate. For 10Ni/CeO_2_673 catalyst, the rate of oxygen transfer from the support to the metal surface is not enough to counter balance the rate of methane decomposition, and carbon accumulates on the surface, in spite of the large amount of oxygen vacancies observed on this catalyst. Once the carbon filaments are formed, the Ni particles are separated from the support, losing the metal-support interface required for the oxygen transfer and the mechanism of carbon removal does not take place any longer. For the 10Ni/CeO_2_1473, the large crystallite size likely leads to a low methane decomposition rate and then, the carbon species formed have time to react with CO_2 from the feed, avoiding carbon deposition

even with low density of oxygen vacancies. It is important to stress that the contact between the very large particles and the support is very low as revealed by *in situ* XANES experiments, which limits the migration of oxygen from the support to the metal surface. These results reveal that the support plays an important role on the mechanism of carbon removal during DRM when small metal particles are present but it is not effective for large metal particles. Damaskinos et al. [65] also reported that the contribution of oxygen from the support to the carbon mechanism removal decreases with the increase in Ni particle size. Djinovic and Pintar [73] also found that significant carbon formation occurs over large NiCo particles regardless the amount of oxygen vacancies of the $CeZrO_2$ support. Djiinovic et al. [74] listed the conditions required for DRM without carbon deposition over a bimetallic NiCo catalyst: (i) a redox support such as $CeZrO_2$ with small crystallite size and high oxygen mobility and (ii) highly dispersed NiCo particles to assure a large interface and a strong interaction between the metal and support. Therefore, for the large Ni particles characteristic of the anodes of SOFC prepared by calcination at high temperature, the redox properties of the support do not improve the resistance of the anodes to carbon formation during DRM reaction due to the reduced metal-support interface that limits the migration of oxygen from the support to the surface of metal particles. The same results were reported for SOFC single cells containing ceria-based catalysts and running on internal ethanol reforming [72].

4. Conclusions

This study investigated the relationship between the Ni particle size and the type and amount of carbon formed over Ni/CeO_2 catalysts for DRM at 1073 K. Furthermore,

the role of a support with redox properties such as CeO_2 on the mechanism of carbon formation for Ni-based catalysts with different particles size was also evaluated.

Ni/CeO_2 catalysts with different Ni loading (5 and 10wt%) and calcination temperature (673, 873, 1073 and 1473 K) were prepared to obtain a wide range of Ni crystallite size. *In situ* XRD and XANES experiments revealed that the calcination temperature affected differently the Ni crystallite size and the number of oxygen vacancies. Increasing the calcination temperature increased the Ni crystallite size, whereas the reducibility of ceria decreased.

The type and the rate of carbon formation during DRM depended on the Ni crystallite size. Both catalysts calcined at 673 K with smaller Ni particle sizes showed the formation of amorphous carbon on the surface of Ni particles. Ni/CeO_2 catalysts with Ni particle size larger than 10 nm exhibited mainly the formation of carbon nanotubes. The rate of carbon deposition increased as the Ni crystallite size increased, achieving a maximum at around 20-30 nm and then, it continuously decreased. However, carbon deposition was negligeable below 10 nm and above 100 nm. These results suggest that methane decomposition is the main reaction pathway for carbon deposition over Ni/CeO_2 catalysts for DRM. For the catalysts with very large Ni crystallite sizes ($10Ni/CeO_2$_1473 and bulk NiO), the CH_4 dissociation rate is likely so low that carbon species formed reacts and carbon accumulation does not occur. These results demonstrate a structure sensitivity of the formation of carbon deposits for DRM reaction.

Most of the studies in the literature report different strategies to produce small Ni particles, which inhibits the deposition of carbon during DRM. However, our work demonstrated that the severe synthesis conditions used on the anode fabrication render this approach inefficient. Therefore, Ni-based SOFC anodes may operate without

significant carbon deposition during DRM since very large Ni particles are formed during anode synthesis. On the other hand, the oxygen mobility of ceria does not contribute to the carbon removal mechanism from the Ni surface due to the low metal-support interface on these large Ni particles.

5. Acknowledgements

The authors thank the Coordenação de Aperfeiçoamento de Pessoal de Nível Superior (CAPES - Finance code 001), the Conselho Nacional de Desenvolvimento Científico e Tecnológico (CNPq - 303667/2018-4; 305046/2015-2; 302469/2020-6; CNPq-SisNANO – 442604/2019-0), and FAPERJ (E-26/010.253/2016; E-26/202.783/2017) for scholarship and financial support. The group thanks the LNLS for the assigned time at D08B-XAFS – 2 (20171082) and XRD1-D12A (20171087) beamlines. This study was also supported by the French government through the Programme Investissement d'Avenir (I-SITE ULNE / ANR-16-IDEX-0004 ULNE) managed by the Agence Nationale de la Recherche. LIA CNRS France-Brazil "Energy & Environment" and Métropole Européen de Lille (MEL) and Region Hauts-de-France for "CatBioInnov" project are also acknowledged.

6. References

(1) N. Laosiripojana, S. Assabumrungrat, Catalytic steam reforming of methane, methanol, and ethanol over Ni/YSZ: The possible use of these fuels in internal reforming SOFC, J. Power Sources. 163 (2007) 943–951. https://doi.org/10.1016/j.jpowsour.2006.10.006.

(2) C. Sun, U. Stimming, Recent anode advances in solid oxide fuel cells, J. Power Sources. 171 (2007) 247–260. https://doi.org/10.1016/j.jpowsour.2007.06.086.

(3) T. Wei, P. Qiu, J. Yang, L. Jia, B. Chi, J. Pu, J. Li, High-performance direct carbon dioxide-methane solid oxide fuel cell with a structure-engineered double-layer anode, J. Power Sources. 484 (2021) 229199–229209. https://doi.org/10.1016/j.jpowsour.2020.229199.

(4) B. Tu, Y. Yin, F. Zhang, X. Su, X. Lyu, M. Cheng, High performance of direct methane-fuelled solid oxide fuel cell with samarium modified nickel-based anode, Int. J. Hydrogen Energy. 45 (2020) 27587–27596. https://doi.org/10.1016/j.ijhydene.2020.07.070.

(5) M. Santoro, I. Luisetto, S. Tuti, S. Licoccia, C. Romano, A. Notargiacomo, E. Di Bartolomeo, Nickel-based structured catalysts for indirect internal reforming of methane, Appl. Sci. 10 (2020) 3083. https://doi.org/10.3390/app10093083.

(6) T. Mishina, N. Fujiwara, S. Tada, A. Takagaki, R. Kikuchi, S.T. Oyama, Calcium-Modified Ni-SDC Anodes in Solid Oxide Fuel Cells for Direct Dry Reforming of Methane, J. Electrochem. Soc. 167 (2020). https://doi.org/10.1149/1945-7111/abba65.

(7) I. Unal, S. Meisuria, M. Choolaei, T.R. Reina, B.A. Horri, Synthesis and characteristics of nanocrystalline $Ni_{1-x}Co_xO$/GDC powder as a methane reforming catalyst for SOFCs, Ceram. Int. 44 (2018) 6851–6860. https://doi.org/10.1016/j.ceramint.2018.01.109.

(8) N.Q. Minh, Ceramic Fuel Cells, J. Am. Ceram. Soc. 76 (1993) 563-588. https://doi.org/10.1111/j.1151-2916.1993.tb03645.x.

(9) A. Atkinson, S. Barnett, R.J. Gorte, J.T.S. Irvine, A.J. Mcevoy, M. Mogensen, S.C. Singhal, J. Vohs, Advanced anodes for high-temperature fuel cells. Nat. Mater. 3 (2004) 17-27. https://doi.org/ 10.1038/nmat1040.

(10) A. Lanzini, P. Leone, C. Guerra, F. Smeacetto, N.P. Brandon, M. Santarelli, Durability of anode supported Solid Oxides Fuel Cells (SOFC) under direct dry-reforming of methane, Chem. Eng. J. 220 (2013) 254–263. https://doi.org/10.1016/j.cej.2013.01.003.

(11) J.R. Rostrup-Nielsen, J. Sehested, J.K. Norskov, Hydrogen and synthesis gas by steam- and CO_2 reforming, Adv. Catal. 47 (2002) 65-139. https://doi.org/10.1016/S0360-0564(02)47006-X.

(12) A. Tarancón, Strategies for lowering solid oxide fuel cells operating temperature, Energies. 2 (2009) 1130–1150. https://doi.org/10.3390/en20401130.

(13) A.L.A. Marinho, R.C. Rabelo-Neto, F. Epron, N. Bion, F.S. Toniolo, F.B. Noronha, Embedded Ni nanoparticles in $CeZrO_2$ as stable catalyst for dry reforming of methane, Appl. Catal. B. 268 (2020) 118387. https://doi.org/10.1016/j.apcatb.2019.118387

(14) M. Li, A.C. van Veen, Tuning the catalytic performance of Ni-catalysed dry reforming of methane and carbon deposition via Ni-CeO2-x interaction, Appl. Catal. B Environ. 237 (2018) 641–648. https://doi.org/10.1016/j.apcatb.2018.06.032.

(15) A.L.A. Marinho, F.S. Toniolo, F.B. Noronha, F. Epron, D. Duprez, N. Bion, Highly active and stable Ni dispersed on mesoporous CeO2-Al2O3 catalysts for production of syngas by dry reforming of methane, Appl. Catal. B Environ. 281 (2021) 119459. https://doi.org/10.1016/j.apcatb.2020.119459.

(16) S.M. Stagg-Williams, F.B. Noronha, G. Fendley, D.E. Resasco, CO2 reforming of CH4 over Pt/ZrO2 catalysts promoted with La and Ce oxides, J. Catal. 194 (2000) 240–249. https://doi.org/10.1006/jcat.2000.2939.

(17) F.B. Noronha, E.C. Fendley, R.R. Soares, W.E. Alvarez, D.E. Resasco, Correlation between catalytic activity and support reducibility in the CO2 reforming of

methane over Pt/CeχZr1-χO2 catalysts, Chem. Eng. J. 82 (2001) 21–31. https://doi.org/10.1016/S1385-8947(00)00368-5.

(18) R.C. Rabelo-Neto, H.B.E. Sales, C.V.M. Inocêncio, E. Varga, A. Oszko, A. Erdohelyi, F.B. Noronha, L. V. Mattos, CO_2 reforming of methane over supported LaNiO3 perovskite-type oxides, Appl. Catal. B Environ. 221 (2018) 349–361. https://doi.org/10.1016/j.apcatb.2017.09.022.

(19) X. Yan, T. Hu, P. Liu, S. Li, B. Zhao, Q. Zhanga, W. Jiao, S. Chen, P. Wang, J. Lu, L. Fan, X. Deng, Y. Pan, Highly efficient and stable Ni/CeO_2-SiO_2 catalyst for dry reforming of methane: Effect of interfacial structure of Ni/CeO_2 on SiO_2, Appl. Catal. B. 246 (2019) 221–231. https://doi.org/10.1016/j.apcatb.2019.01.070.

(20) I. Luisetto, S. Tuti, C. Romano, M. Boaro, E. Di Bartolomeo, Dry reforming of methane over Ni supported on doped CeO 2 : New insight on the role of dopants for CO_2 activation, J. CO_2 Util. 30 (2019) 63–78. https://doi.org/10.1016/j.jcou.2019.01.006.

(21) S. Aghamohammadi, M. Haghighi, M. Maleki, N. Rahemi, Sequential impregnation vs. sol-gel synthesized Ni/Al_2O_3-CeO_2 nanocatalyst for dry reforming of methane: Effect of synthesis method and support promotion, Mol. Catal. 431 (2017) 39–48. https://doi.org/10.1016/j.mcat.2017.01.012.

(22) G. Bonura, C. Cannilla, F. Frusteri, Ceria–gadolinia supported NiCu catalyst: A suitable system for dry reforming of biogas to feed a solid oxide fuel cell (SOFC), Appl. Catal. B. 121 (2012) 135-147. https://doi.org/10.1016/j.apcatb.2012.03.028.

(23) C. Gaudillère, P. Vernoux, C. Mirodatos, G. Caboche, D. Farrusseng, Screening of ceria-based catalysts for internal methane reforming in low temperature SOFC, Catal. Today. 157 (2010) 263-269. https://doi.org/10.1016/j.cattod.2010.02.062.

(24) R.O. Da Fonseca, A.A.A. Da Silva, M.R.M. Signorelli, R.C. Rabelo-Neto, F.B. Noronha, R.C.C. Simões, L. V. Mattosa, Nickel / doped ceria solid oxide fuel cell anodes for dry reforming of methane, J. Braz. Chem. Soc. 25 (2014) 2356–2363. https://doi.org/10.5935/0103-5053.20140245.

(25) V. Modafferi, G. Panzera, V. Baglio, F. Frusteri, P.L. Antonucci, Propane reforming on Ni-Ru/GDC catalyst: H2 production for IT-SOFCs under SR and ATR conditions, Appl. Catal. A Gen. 334 (2008) 1–9. https://doi.org/10.1016/j.apcata.2007.10.006.

(26) A.A.A. Da Silva, N. Bion, F. Epron, S. Baraka, F.C. Fonseca, R.C. Rabelo-Neto, L.V. Mattos, F.B. Noronha, Effect of the type of ceria dopant on the performance of Ni/CeO_2 SOFC anode for ethanol internal reforming, Appl. Catal. B 206 (2017) 626–641. https://doi.org/10.1016/j.apcatb.2017.01.069.

(27) J.L.M. Rupp, A. Infortuna, L.J. Gauckler, Microstrain and self-limited grain growth in nanocrystalline ceria ceramics, Acta Mater. 54 (2006) 1721–1730. https://doi.org/10.1016/j.actamat.2005.11.032.

(28) G.K. Williamson, W.H. Hall, X-ray line broadening from filed aluminium and wolfram, Acta Metall. 1 (1953) 22–31. https://doi.org/10.1016/0001-6160(53)90006-6.

(29) W.Y. Hernandez, O.H. Laguna, M.A. Centeno, J.A. Odriozola, Structural and catalytic properties of lanthanide (La, Eu, Gd) doped ceria, J. Solid State Chem. 184 (2011) 3014-3020. https://doi.org/10.1016/j.jssc.2011.09.018.

(30) I. Kosacki, T. Suzuki, H.U. Anderson, P. Colomban, P, Raman scattering and lattice defects in nanocrystalline CeO_2 thin films, Solid State Ion. 149 (2002) 99-105. https://doi.org/10.1016/S0167-2738(02)00104-2.

(31) R.O. Da Fonseca, R.C. Rabelo-Neto, R.C.C. Simões, L. V. Mattos, F.B. Noronha, Pt supported on doped CeO_2/Al_2O_3 as catalyst for dry reforming of methane,

Int. J. Hydrogen Energy. 45 (2020) 5182–5191. https://doi.org/10.1016/j.ijhydene.2019.09.207.

(32) J.E. Spanier, R.D. Robinson, F. Zhang, S.W. Chan, I.P. Herman, Size-dependent properties of CeO_{2-y} nanoparticles as studied by Raman scattering, Phys. Rev. B 64 (2001) 245407. https://doi.org/10.1103/PhysRevB.64.245407.

(33) J. Yu, Q. Cao, Y. Li, X. Long, S. Yang, J.K. Clark, M. Nakabayashi, M. Shibata, J.J. Delaunay, Defect-Rich $NiCeO_x$ Electrocatalyst with Ultrahigh Stability and Low Overpotential for Water Oxidation, ACS Catal. 9 (2019) 1605-1611. https://doi.org/10.1021/acscatal.9b00191.

(34) P.H. Ho, G.S. De Luna, A. Poggi, M. Nota, E. Rodriguez-Castellón, G. Fornasari, A. Vaccari, P. Benito, Ru–CeO_2 and Ni–CeO_2 Coated on Open-Cell Metallic Foams by Electrodeposition for the CO_2 Methanation, Ind. Eng. Chem. Res. 60 (2021) 6730-6741. https://doi.org/10.1021/acs.iecr.0c06024.

(35) G. Basina, K. Polychronopoulou, A.F. Zedan, K. Dimos, M.S. Katsiotis, A.P. Fotopoulos, I. Ismail, V. Tzitzios, Ultrasmall Metal-Doped CeO_2 Nanoparticles for Low-Temperature CO Oxidation, ACS Appl. Nano Mater. 3 (2020) 10805-10813. https://doi.org/10.1021/acsanm.0c02090.

(36) W. Derafa, F. Paloukis, B. Mewafy, W. Baaziz, O. Ersen, C. Petit, G. Corbel, S. Zafeiratos, Synthesis and characterization of nickel-doped ceria nanoparticles with improved surface reducibility, RSC Adv., 8 (2018) 40712–40719. https://doi.org/10.1039/c8ra07995a.

(37) E. Poggio-Fraccari, B. Irigoyen, G. Baronetti, F. Mariño, Ce-Pr mixed oxides as active supports for Water-gas Shift reaction: Experimental and density functional theory characterization, Appl. Catal. A. 485 (2014) 123-132. https://doi.org/10.1016/j.apcata.2014.07.040.

(38) J.R. MCBride, K.C. Hass, B.D. Poindexter, W.H. Weber, Raman and x-ray studies of $Ce_{1-x}RE_xO_{2-y}$, where RE=La, Pr, Nd, Eu, Gd, and Tb, J. Appl. Phys. 76 (1994) 2435. https://doi.org/10.1063/1.357593.

(39) L. Barrio, A. Kubacka, G. Zhou, M. Estrella, A. Martinez-Arias, J.C. Hanson, M. Fernadez-Garcia, J.A. Rodriguez, Unusual Physical and Chemical Properties of Ni in $Ce_{1-x}Ni_xO_{2-y}$ Oxides: Structural Characterization and Catalytic Activity for the Water Gas Shift Reaction, J. Phys. Chem. C. 114 (2010) 12689-12697. https://doi.org/10.1021/jp103958u.

(40) N. Yisup, Y. Cao, W.L. Feng, W.L. Dai, K.N Fan, Catalytic oxidation of methane over novel Ce–Ni–O mixed oxide catalysts prepared by oxalate gel-coprecipitation, Catal. Letters 99 (2005) 207-213. https://doi.org/10.1007/s10562-005-2121-9.

(41) W. Xu, R. Si, S.D. Senanayake, J. Llorca, H. Idriss, D. Stacchiola, J.C. Hanson, J.A. Rodriguez, *In situ* studies of CeO_2-supported Pt, Ru, and Pt–Ru alloy catalysts for the water–gas shift reaction: Active phases and reaction intermediates, J. Catal. 291(2012) 117–126. https://doi.org/10.1016/j.jcat.2012.04.013.

(42) W. Xu, Z. Liu, A.C. Johnston-Peck, S.D. Senanayake, G. Zhou, D. Stacchiola, E.A. Stach, J.A. Rodriguez, Steam Reforming of Ethanol on Ni/CeO_2: Reaction Pathway and Interaction between Ni and the CeO_2 Support, ACS Catal. 3 (2013) 975–984. https://doi.org/10.1021/cs4000969.

(43) F. Zhang, Z. Liu, X. Chen, N. Rui, L.E. Betancourt, L. Lin, W. Xu, C. Sun, A.M.M. Abeykoon, J.A. Rodriguez, J. Teržan, K. Lorber, P. Djinović, S.D. Senanayake, Effects of Zr Doping into Ceria for the Dry Reforming of Methane over $Ni/CeZrO_2$ Catalysts: In Situ Studies with XRD, XAFS, and AP-XPS, ACS Catal. 19 (2020) 3274−3284. https://dx.doi.org/10.1021/acscatal.9b04451

(44) M.F. Bekheet, M. Grünbacher, L. Schlicker, A. Gili, A. Doran, J.D. Epping, A. Gurlo, B. Klötzer, S. Penner, On the structural stability of crystalline ceria phases in undoped and acceptor-doped ceria materials under in situ reduction condition, Cryst. Eng. Comm. 21 (2019) 145-154. https://doi.org/10.1039/C8CE01726C.

(45) RJ. Gaboriaud, F. Paumier, B. Lacroix, Disorder-order phase transformation in a fluorite-related oxide thin film: In-situ X-ray diffraction and modeling of the residual stress effects, Thin Solid Films. 601 (2016) 84-88. https://doi.org/10.1016/j.tsf.2015.08.030.

(46) F. Vasiliu, V. Pârvulescu, C. Sârbu, Trivalent Ce_2O_3 and CeO_{2-x} intermediate oxides induced by laser irradiation of CeO_2 powders, J. Mater. Sci. 29 (1994) 2095-2101. https://doi.org/10.1007/BF01154685.

(47) Z. Wang, X. Hu, D. Dong, G. Parkinson, C.Z. Li, Effects of calcination temperature of electrospun fibrous Ni/Al_2O_3 catalysts on the dry reforming of methane, Fuel Process. Technol. 155 (2017) 246-251. https://doi.org/10.1016/j.fuproc.2016.08.001

(48) J. El Fallah, S. Boujana, H. Dexpert, A. Kiennemann, J. Majerus, O. Touret, F. Villain, F. Le Normand, Redox Processes on Pure Ceria and on Rh/CeO_2 Catalyst Monitored by X-Ray Absorption (Fast Acquisition Mode), J. Phys. Chem. 98 (1994) 5522-5533. https://doi.org/10.1021/j100072a020.

(49) M.G. Zimicz, S.A. Larrondo, R.J. Prado, D.G. Lamas, Time-resolved in situ XANES study of the redox properties of $Ce_{0.9}Zr_{0.1}O_2$ mixed oxides, Int. J. Hydrogen Energy. 37 (2012) 14881–14886. https://doi.org/10.1016/j.ijhydene.2012.01.162.

(50) M.C. Ribeiro, R.C. Rabelo-Neto, L. V. Mattos, G. Jacobs, B.H. Davis, F.B. Noronha, A relationship between the production of oxygenates from ethanol/steam

mixtures and the oxygen mobility in transition metal oxide doped $CeO_2 \cdot SiO_2$ catalysts, J. Phys. Chem. C. 118 (2014) 28007–28016. https://doi.org/10.1021/jp509533g.

(51) A. Norman, V. Perrichon, A. Bensaddik, S. Lemaux, H. Bitter, D. Koningsberger, Study of the reducibility of Pt or Pd on ceria-zirconia catalysts by XANES measured at the Ce L_{III} edge and magnetic susceptibility measurements, Top. Catal. 16–17 (2001) 363–368. https://doi.org/10.1023/a:1016621401560.

(52) H.C. Yao, Y.F.J. Yao, Ceria in automotive exhaust catalysts: I. Oxygen storage, J. Catal. 86 (1984) 254–265. https://doi.org/10.1016/0021-9517(84)90371-3.

(53) J.Z. Shyu, K. Otto, Characterization of Pt/γ-alumina catalysts containing ceria, J. Catal. 115 (1989) 16–23. https://doi.org/10.1016/0021-9517(89)90003-1.

(54) J. Kaspar, P. Fornasiero, M. Graziani, Use of CeO_2-based oxides in the three-way catalysis, Catal. Today 50 (1999) 285-298. https://doi.org/10.1016/S0920-5861(98)00510-0.

(55) D.S. Lee, D.J. Min, A Kinetics of Hydrogen Reduction of Nickel Oxide at Moderate Temperature, Met. Mater. Int. 25 (2019) 982-990. https://doi.org/10.1007/s12540-019-00261-y.

(56) J. Dang, K.C. Chou, X.J. Hu, G.H. Zhang, Reduction Kinetics of Metal Oxides by Hydrogen, Steel Res. Int. 84 (2013) 526-533. https://doi.org/10.1002/srin.201200242.

(57) V.M. Gonzalez-Dela Cruz, J.P. Holgado, R. Pereñíguez, A. Caballero, Morphology changes induced by strong metal-support interaction on a Ni-ceria catalytic system, J. Catal. 257 (2008) 307–314. https://doi.org/10.1016/j.jcat.2008.05.009

(58) W.J. Jang, J.O. Shim, H.M. Kim, S.Y. Yoo, H.S. Roh, A review on dry reforming of methane in aspect of catalytic properties, Catal. Today. (2019) 15–26. https://doi.org/10.1016/j.cattod.2018.07.032.

(59) N.A.K. Aramouni, J.G. Touma, B.A. Tarboush, J. Zeaiter, M.N. Ahmad, Catalyst design for dry reforming of methane: Analysis review, Renew. Sustain. Energy Rev. 82 (2018) 2570–2585. https://doi.org/10.1016/j.rser.2017.09.076.

(60) G. Zhang, J. Liu, Y. Xu, Y. Sun, A review of CH4–CO2 reforming to synthesis gas over Ni-based catalysts in recent years (2010–2017), Int. J. Hydrogen Energy. 43 (2018) 15030–15054. https://doi.org/10.1016/j.ijhydene.2018.06.091.

(61) J.R. Rostrup-Nielsen, T. Rostrup-Nielsen, Large-Scale Hydrogen Production, Cattech 6 (2002) 150–159. https://doi.org/10.1023/A:1020163012266.

(62) D.L. Trimm, Coke formation and minimisation during steam reforming reactions, Catal. Today. 37 (1997) 233–238. https://doi.org/10.1016/S0920-5861(97)00014-X.

(63) D.L. Trimm, Catalysts for control of coking during steam reforming, Catal. Today 49 (1999) 3-10. https://doi.org/10.1016/S0920-5861(98)00401-5.

(64) B. Kitiyanan, W.E. Alvarez, J.H. Harwell, D.E. Resasco, Controlled production of single-wall carbon nanotubes by catalytic decomposition of CO on bimetallic Co–Mo catalysts, Chem. Phys. Lett. 317 (2000) 497–503. https://doi.org/10.1016/S0009-2614(99)01379-2.

(65) C.M. Damaskino, J. Zavasnik, P. Djinovic, A.M. Efstathiou, Dry reforming of methane over Ni/$Ce_{0.8}Ti_{0.2}O_{2-\delta}$: The effect of Ni particle size on the carbon pathways studied by transient and isotopic techniques, Appl. Catal. B. 296 (2021) 120321-120341. https://doi.org/10.1016/j.apcatb.2021.120321.

(66) C. Vogt, J. Kranenborg, M. Monai, B.M. Weckhuysen, Structure Sensitivity in Steam and Dry Methane Reforming over Nickel: Activity and Carbon Formation, ACS Catal. 10 (2020) 1428–1438. https://doi.org/10.1021/acscatal.9b04193.

(67) H.S. Bengaard, J.K. Nørskov, J. Sehested, B.S. Clausen, L.P. Nielsen, A.M. Molenbroek, J.R. Rostrup-Nielsen, Steam Reforming and Graphite Formation on Ni Catalysts, J. Catal. 209 (2002) 365–384. https://doi:10.1006/jcat.2002.3579

(68) Y. Li, D. Li, G. Wang, Methane decomposition to CO_x-free hydrogen and nano-carbon material on group 8-10 base metal catalysts: A review, Catal. Today. 162 (2011) 1–48. https://doi.org/10.1016/j.cattod.2010.12.042.

(69) H. Dai, A.G. Rinzler, P. Nikolaev, A. Thess, D.T. Colbert, R.E. Smalley, Single-wall nanotubes produced by metal-catalyzed disproportionation of carbon monoxide, Chem. Phys. Lett. 260 (1996) 471-475. https://doi.org/10.1016/0009-2614(96)00862-7.

(70) D. Chen, K.O. Christensen, E. Ochoa-Fernández, Z. Yu, B. Tøtdal, N. Latorre, A. Monzón, A. Holmen, Synthesis of carbon nanofibers: Effects of Ni crystal size during methane decomposition, J. Catal. 229 (2005) 82–96. https://doi.org/10.1016/j.jcat.2004.10.017.

(71) M.L. Toebes, J.H. Bitter, A.J.V. Dillen, K.P. De Jong, Impact of the structure and reactivity growth of carbon nanofibers, Catal. Today 76 (2002) 33-42. https://doi.org/10.1016/S0920-5861(02)00209-2.

(72) A.A.A. Da Silva, M.C. Steil, F.N. Tabuti, R.C. Rabelo-Neto, F.B. Noronha, L.V. Mattos, The role of the ceria dopant on Ni/doped-ceria anodic layer cermets for direct ethanol solid oxide fuel cell, Int. J. Hydrog. Energy 46 (2021) 4309-4328. https://doi.org/10.1016/j.ijhydene.2020.10.155.

(73) P. Djinovic, A. Pintar, Stable and selective syngas production from dry CH_4-CO_2 streams over supported bimetallic transition metal catalysts, Appl. Catal. B: Environ. 206 (2017) 675–682. http://dx.doi.org/10.1016/j.apcatb.2017.01.064.

(74) P. Djinovic, I.G.O. Crnivec, B. Erjavec, A. Pintar, Influence of active metal loading and oxygen mobility on coke-free dry reforming of Ni–Co bimetallic catalysts,

Appl. Catal. B: Environ. 125 (2012) 259– 270. http://dx.doi.org/10.1016/j.apcatb.2012.05.049.

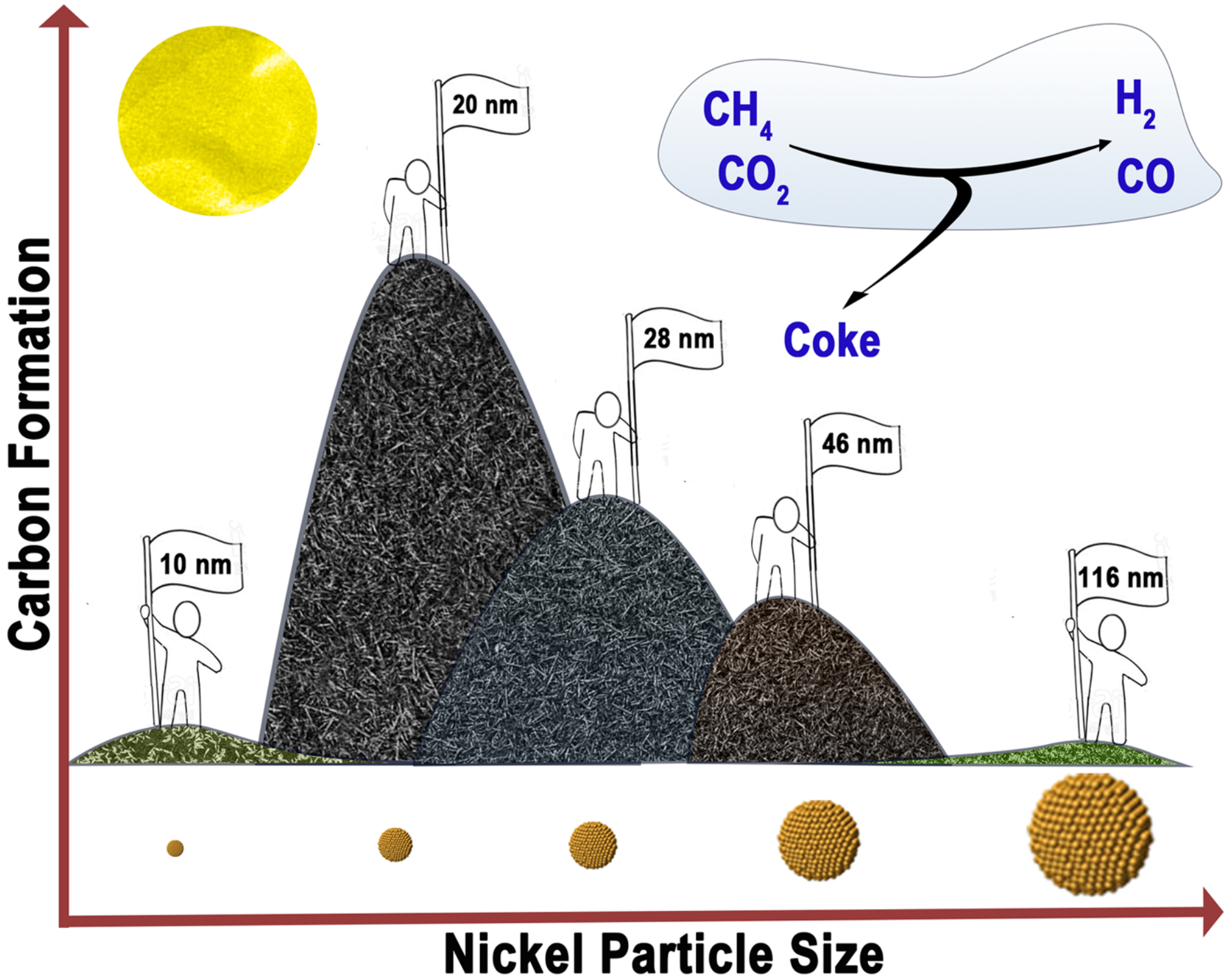
Carbon Formation
Nickel Particle Size
CH_4
CO_2
H_2
CO
Coke
10 nm
20 nm
28 nm
46 nm
116 nm